

## Proper Motions of the Jets in the Region of HH 30 and HL/XZ Tau. Evidence for a Binary Exciting Source of the HH 30 Jet

Guillem Anglada<sup>1</sup>, Rosario López<sup>2</sup>, Robert Estalella<sup>2</sup>, Josefa Masegosa<sup>1</sup>, Angels Riera<sup>2,3</sup>,  
and Alejandro C. Raga<sup>4</sup>

### ABSTRACT

We present [SII] images of the HH 30 and HL/XZ Tau region obtained at two epochs, as well as long-slit optical spectroscopy of the HH 30 jet. We measured proper motions of  $\sim 100\text{--}300\text{ km s}^{-1}$  for the HH 30 jet and counterjet, and of  $\sim 120\text{ km s}^{-1}$  for the HL Tau jet. Inclination angles with respect to the plane of the sky are  $0^\circ\text{--}40^\circ$  for the HH 30 jet and  $60^\circ$  for the HL Tau jet. Comparison with previous observations suggests that most of the jet knots consist of persisting structures. Also, we corroborate that the HH 30-N knots correspond to the head of the HH 30 jet. The overall HH 30 jet structure can be well described by a wiggling ballistic jet, arising either by the orbital motion of the jet source around a primary or by precession of the jet axis because of the tidal effects of a companion. In the first scenario, the orbital period would be 53 yr and the total mass  $0.25\text{--}2 M_\odot$ . In the precession scenario, the mass of the jet source would be  $\sim 0.1\text{--}1 M_\odot$ , the orbital period  $< 1$  yr, and the mass of the companion less than a few times  $0.01 M_\odot$ , thus being a substellar object or a giant exoplanet. In both scenarios a binary system with a separation  $< 18\text{ AU}$  ( $< 0''.13$ ) is required. Since the radius of the flared disk observed with the *HST* is  $\sim 250\text{ AU}$ , we conclude that this disk appears to be circumbinary rather than circumstellar, suggesting that the search for the collimating agent of the HH 30 jet should be carried out at much smaller scales.

---

<sup>1</sup> Instituto de Astrofísica de Andalucía, CSIC, Camino Bajo de Huétor 50, E-18008 Granada, Spain; guillem@iaa.es, pepa@iaa.es

<sup>2</sup> Departament d'Astronomia i Meteorologia, Universitat de Barcelona, Av. Diagonal 647, E-08028 Barcelona, Spain; rosario.lopez@am.ub.es, robert.estalella@am.ub.es

<sup>3</sup> Departament de Física i Enginyeria Nuclear, Universitat Politècnica de Catalunya, Vilanova i la Geltrú, Spain; angels.riera@upc.es

<sup>4</sup> Instituto de Ciencias Nucleares, UNAM, Apdo. Postal 70-543, 04510 México D.F., Mexico; raga@nucleares.unam.mx

*Subject headings:* ISM: Herbig-Haro objects — ISM: individual (HH 30, HH 266) — ISM: jets and outflows — stars: formation — stars: individual (HL Tau, XZ Tau)

## 1. Introduction

The region encompassing the Herbig-Haro (HH) object 30 and the stars HL/XZ Tau, in the northeastern part of the L1551 dark cloud, lies at a distance of 140 pc (e.g., Kenyon et al. 1994). It is particularly rich in HH jets, being one of the regions where this phenomenon was first identified (Mundt & Fried 1983).

The HH 30 outflow is considered a prototypical jet/disk system. It presents a clear jet/counterjet structure, which has been described, e. g., by Mundt et al. (1987, 1988) and by Graham & Heyer (1990). The HH 30 exciting source is an optically invisible star (Vrba, Rydgren, & Zak 1985) highly extinguished by an edge-on disk (Burrows et al. 1996, Stapelfeldt et al. 1999), that extends up to a radius of  $\sim 250$  AU perpendicularly to the jet, and divides the surrounding reflection nebulosity into two lobes. Kenyon et al. (1998) propose a spectral type M0 for the HH 30 star, and Cotera et al. (2001) estimate a bolometric luminosity of 0.2–0.9  $L_{\odot}$ . López et al. (1995, 1996) argue that a number of knots located to the northeast of the HH 30 object are possibly also part of the same flow, resulting in a total angular size of  $\sim 7'$  for the whole outflow. Several studies have explored the spatial morphology (both along and across the symmetry axis; Mundt et al. 1991, Ray et al. 1996), line ratios (Mundt et al. 1990; Bacciotti, Eisloffel, & Ray 1999), radial velocities (Raga et al. 1997), and proper motions (Mundt et al. 1990; Burrows et al. 1996; López et al. 1996) of the HH 30 flow.

HL Tau, located  $\sim 1'.5$  north from the HH 30 source, has been one of the most intensively studied T Tauri stars. Since the first proposal that this star is associated with a nearly edge-on circumstellar disk (Cohen 1983), numerous studies have been carried out in order to image the proposed disk (e.g., Sargent & Beckwith 1987, 1991; Lay et al. 1994; Lay, Carlstrom, & Hills 1997; Rodríguez et al. 1994; Mundy et al. 1996; Wilner, Ho, & Rodríguez 1996; Looney, Mundy & Welch 2000), although recent studies suggest that the flattened molecular structure around HL Tau is part of a larger molecular shell-like structure (Welch et al. 2000). This star has been proposed as the source of a molecular outflow (Calvet, Cantó & Rodríguez 1983; Torrelles et al. 1987; Monin, Pudritz, & Lazareff 1996). HL Tau is also the source of a collimated jet/counterjet system, that has been extensively studied (e.g., Mundt et al. 1987, 1988, 1990, 1991, Rodríguez et al. 1994). López et al. (1995, 1996), on the basis of geometrical alignment and proper motion measurements, propose that HH 266, an extended structure  $\sim 4'$  to the northeast of HL Tau, might correspond to the head of the HL Tau jet.

XZ Tau, located  $\sim 25''$  to the east of HL Tau, is a close binary system composed of a T Tauri star and a cool companion separated by  $0''.3$  (Haas, Leinert, & Zinnecker 1990). XZ Tau is also the source of an optical outflow, as revealed, e.g., by the studies of Mundt et al. (1988, 1990), and more recently by direct evidence of the expansion of the nebular emission, moving away from XZ Tau, in the spectacular sequence of *HST* images of Krist et al. (1999). XZ Tau has also been proposed as an alternative driving source for the molecular high-velocity gas observed towards the HL/XZ Tau complex (Torrelles et al. 1987), and is located at the center of the ring- or shell-shaped molecular structure imaged by Welch et al. (2000).

Despite the numerous studies carried out in this region, proper motions have only been measured for a relatively small number of knots of the HH jets present in this region, using images obtained under quite unequal conditions (different filters, sensitivities or telescopes). Mundt et al. (1990) measured proper motions for one knot of the HH 30 jet, and five additional knots near HL/XZ Tau by comparing a Gunn  $r$  filter image with a [SII]+H $\alpha$  image, separated by an interval of four years; Burrows et al. (1996) measured proper motions for the small scale structure of knots in the HH 30 jet/counterjet from two *HST* F675W images (including [SII], H $\alpha$ , and [OI] lines) separated by one year, but because of differences in sensitivity between both images, proper motion measurements were restricted to the region within  $5''$  from the star; finally, López et al. (1996) obtained proper motions for five knots of the HH 30 jet, and for HH 266, from two [SII] images separated by about one year, but obtained with different instrumentation.

In the present paper, we used sensitive CCD frames obtained at two epochs with the same instrument, in order to make a detailed study of the proper motions along the region. Our observations are complementary to those carried out with the *HST* telescope, since the *HST* covers with very high angular resolution the brightest region near (a few arcsec) the exciting sources, while our observations cover a much more extended, low brightness region, up to  $\sim 5'$  from the exciting sources. We measured proper motions for a number of knots much larger than in previous studies, in order to obtain the full kinematics of the region. Given the proximity of the region ( $D = 140$  pc), a time span of one year between the two images allowed us to measure the proper motions with enough accuracy, and made easier the identification of the knots. We compared our proper motion results with those obtained in previous studies in order to obtain the time evolution of the jet structures.

For the HH 30 jet, we have also carried out high resolution spectroscopy to measure the radial velocity along the jet, in order to obtain the full kinematics of this object.

The paper is organized as follows. The observations and procedures used to measure the proper motions are described in § 2. In § 3 we present the results we obtained from our

proper motion and spectroscopic measurements and we compare them with those of previous observations reported in the literature. In § 4 we discuss the origin of the HH 30 jet wiggling structure in terms of orbital motions of the jet source and precession of the jet axis; we also discuss the large-scale structure of the HH 30 jet. In § 5 we give our conclusions.

## 2. Observations and Data Analysis

### 2.1. CCD Imaging

CCD images of the HL Tauri region, including the HH 30 jet and the HH 30-N and HH 266 emission structures, were obtained at two different epochs (1998 November 20 and 1999 November 8). The observations were made with the 2.5 m Nordic Optical Telescope (NOT) at the Observatorio del Roque de los Muchachos (La Palma, Spain). The same setup was used for the two runs. The images were obtained with the Andalucia Faint Object Spectrograph and Camera (ALFOSC), equipped with a Ford-Loral CCD with  $2048 \times 2048$  pixels with an image scale of  $0''.188 \text{ pixel}^{-1}$ . A square filter, with a central wavelength  $\lambda = 6720 \text{ \AA}$  and bandpass  $\Delta\lambda = 56 \text{ \AA}$  (that includes the red [SII] 6717, 6731  $\text{\AA}$  lines) was used for these observations. On the NOT, the nominal ALFOSC field is  $6'.5 \times 6'.5$ . However, because of the square geometry of the [SII] filter used and the misalignment with the CCD axes, the effective field sampled through the filter was only  $\sim 5' \times 5'$ .

The images were processed with the standard tasks of the IRAF<sup>1</sup> reduction package. Individual frames were recentered using the reference positions of several field stars, in order to correct for the misalignments among them.

The “first epoch” NOT image was obtained by combining five frames of 1800 s exposure each, in order to get a deep [SII] image of 2.5 h of integration time. Typical values of seeing for individual frames were  $1''\text{--}1''.2$ , resulting in a seeing of  $1''$  for the final “first epoch” image. The “second epoch” NOT image was obtained by combining eight frames of 1800 s exposure each in order to get a final image with a total integration time of 4 h. For this second epoch, the typical values of seeing for individual frames were  $0''.7\text{--}1''$ , resulting in a seeing of  $0''.7$  for the final “second epoch” image.

Images were not flux-calibrated. However, we have performed aperture photometry of comon field stars on the images of the two epochs and we estimate that the deepness of the

---

<sup>1</sup>IRAF is distributed by the National Optical Astronomy Observatories, which are operated by the Association of Universities for Research in Astronomy, Inc., under cooperative agreement with the National Science Foundation.

two images differs by less than 0.5 mag in the filter used.

## 2.2. Measurement of Proper Motions

To measure the proper motions, the first- and second-epoch [SII] CCD final images were converted into a common reference system by using the positions of eleven field stars plus the position of the HH 30 star. The  $y$  axis is oriented at a position angle (P.A.) of  $30^\circ 6'$ , roughly coincident with the HH 30 jet axis. The GEOMAP and GEOTRAN tasks of IRAF were used to perform a linear transformation with six free parameters taking into account relative translation, rotations and magnifications between frames. After the transformation, the average and rms of the difference in position for the reference stars in the two images was  $-0.08 \pm 0.34$  pixels in the  $x$  coordinate and  $-0.18 \pm 0.21$  pixels in the  $y$  coordinate.

In order to improve the signal-to-noise ratio of the diffuse knot structures, the aligned images were convolved with Gaussian filters using the GAUSS IRAF task. For the knots nearest to the HH 30 star (i.e., knots A–D and counterjet), a Gaussian filter with a FWHM of  $0''.36$  was applied to both images. For the rest of the knots the Gaussian filter applied to the images had a FWHM of  $0''.63$ .

We defined boxes that included the emission of the individual condensations in each epoch, we computed the two-dimensional cross-correlation function of the emission within the boxes, and finally we determined the proper motion through a parabolic fit to the peak of the cross-correlation function (see the description of this method in Reipurth et al. 1992, and López et al. 1996). The uncertainty in the position of the correlation peak has been estimated through the scatter of the correlation peak positions obtained from boxes differing from the nominal one in 0 or  $\pm 2$  pixels ( $0''.38$ ) in any of its four sides, making a total  $3^4 = 81$  different boxes for each knot. The error adopted has been twice the rms deviation of position, for each coordinate, added quadratically to the rms alignment error.

For the knots near the HH 30 source (knots A–D and counterjet), the intensity gradient in the jet direction made unreliable the usage of the correlation method. For this region, we integrated the emission across the jet over a width of 11 pixels ( $2''.1$ ) and identified the position of each knot along the jet through a parabolic fit after baseline removal. A similar procedure, but integrating the emission along the jet for a typical width of 6 pixels ( $1''.1$ ) at the position of each knot, allowed us to measure the  $x$  coordinate of the knots. For these knots we estimated that the major source of error was the residual misalignment of the two images, and the uncertainty adopted for the proper motions was  $\sqrt{2}$  times the rms alignment error for each coordinate. However, we cannot discard that residual contamination from continuum

emission constitutes an additional source of uncertainty in our proper motion measurements of the knots nearest to the HH 30 source.

### 2.3. Optical Spectroscopy

Optical spectroscopy of the HH 30 jet and HH 30-N was acquired during 1998 December 11 and 12 using the red arm of the double-armed spectrograph ISIS (Carter et al. 1994), and a Tektronics CCD detector of  $1024 \times 1024$  pixels, at the Cassegrain focus of the 4.2 m William Herschel Telescope (WHT) at the Observatorio del Roque de los Muchachos (La Palma, Spain). The high resolution grating R1200R (dispersion of  $0.41 \text{ \AA pixel}^{-1}$ ), centered at  $6600 \text{ \AA}$  and covering a wavelength range of  $420 \text{ \AA}$  (that includes the  $H\alpha$  and [SII] 6717, 6731  $\text{\AA}$  lines), was employed. The effective spectral resolution achieved was  $0.7 \text{ \AA}$  ( $\sim 32 \text{ km s}^{-1}$ ). The angular scale was  $0''.36 \text{ pixel}^{-1}$ .

In order to obtain the spectrum of the HH 30 jet, the  $3''.7$  long slit was centered on the HH 30 star with a P.A. of  $30^\circ$ . One exposure of 600 s of the HH 30 jet was obtained on 1998 December 12, with a slit width of  $1''.5$ . Four exposures of 1800 s each, with a total integration time of 2 h, were obtained on 1998 December 11 through HH 30-N. The slit was centered on the position of knot NE (López et al. 1996), at a P.A. of  $30^\circ$ , covering the emission from knots NA to NH.

The data were reduced using the standard procedures for the long-slit spectroscopy within the IRAF package. The spectra were not flux-calibrated. The line-of-sight velocity as a function of position along the HH 30 jet and HH 30-N has been obtained by fitting multiple Gaussians to the observed [SII] 6717, 6731  $\text{\AA}$  and  $H\alpha$  emission line profiles, using the SPLOT task of IRAF. The Gaussian profiles are described in terms of line center, which is transformed into heliocentric velocity, and line width, given as the full width at half maximum (FWHM).

## 3. Results

### 3.1. Overall Description

In Figure 1 we show the [SII] image of the overall region, about  $5'$  in size, corresponding to the first epoch. The field includes the HH 30 source, near the southern edge of the image, which appears at the vertex of a cone of nebulosity that apparently extends along several tens of arcsec. The HH 30 jet crosses the image from southwest to northeast, and its wiggling

as it propagates away from its exciting source is clearly visible. The image also includes the HH 30-N knots, near the northern edge of the image, which have been proposed to also belong to the HH 30 jet (López et al. 1995). Unfortunately only the very first knots of the HH 30 counterjet fall inside the field.

The bright stars HL and XZ Tau and their associated jets are also included in the observed field. A large fraction of the HL Tau counterjet is visible in the southwestern part of the image, while the HH 266 object, proposed to be also associated with HL Tau (López et al. 1995) falls near the northeastern corner of the image. The young stellar object LkH $\alpha$  358 is also visible near the western edge of the image.

Faint knots, corresponding to the emission-line knots K1-K3 identified by Mundt et al. (1988) (see their Fig. 1), can be seen in our images  $\sim 30''$  to the southeast of XZ Tau. Additional knots, extending  $\sim 40''$  to the east of K1-K3 can also be seen in our images. These knots are connected by diffuse emission that extends further away, forming an apparent “ring” with a radius of  $\sim 1'.5$ , surrounding the darker region observed towards the center of the frame. We detected these knots and the diffuse emission in our images at the two epochs, but we did not find evidence for systematic proper motions. Thus, this apparent ring probably arises as a result of an increase in extinction towards the center of the field, because of a foreground clump. It is interesting to note that a molecular ring, centered near XZ Tau, has been mapped in  $^{13}\text{CO}$  by Welch et al. (2000). The dark region at the center of our image coincides with the eastern side of the molecular ring, suggesting that this dark region corresponds to the increase of extinction because of this foreground molecular cloud, with the diffuse optical emission probably originating at the edges of this molecular structure. HL Tau falls close to the western side of the molecular ring and, as noted by Welch et al. (2000), the large arc of scattered light that appears to pass through HL Tau, apparently corresponds to the western side of the molecular structure.

## 3.2. HH 30

### 3.2.1. Proper Motions

In Table 1 and Figure 2 we give the proper motion results obtained for the HH 30 jet using the procedures described in §2.2. The proper motion velocity has been calculated assuming a distance of 140 pc. In the proper motion calculations, the  $y$  axis is at a position angle of  $30^\circ 6'$ , in the approximate direction of the jet. We have set the zero point of our coordinate system on the bright knot closest to the HH 30 star, labeled as A0. We identified this knot with the knot 95-01N of the *HST* image of Burrows et al. (1996). These authors

estimate from a fit of the *HST* image to a flared disk using scattered-light models that the position of the exciting source is shifted from 95-01N, corresponding to a position  $y = -0''.51$ .

The nomenclature used for the knots maintains the single letter names used by Mundt et al. (1990) and López et al. (1995). However, the number after the letter indicates only an order of distance from the HH 30 star and no attempt has been made to be consistent with previous observations. Thus, for instance, the group of knots B is roughly at the same distance from the HH 30 source in the images of Mundt et al. (1990), López et al. (1995), and in this paper; however, knots B1, B2, and B3 identified in the present images do not have a clear correspondence with knots B1 and B2 of Mundt et al. (1990) (see the discussion below).

The proper motion velocities obtained along the HH 30 jet range from  $\sim 100$  to  $\sim 300$  km s $^{-1}$ , in a direction close to the jet axis. Near the source the velocities appear to be higher, with velocities of  $\sim 200$  to  $\sim 300$  km s $^{-1}$  for knots A to D (corresponding to distances from  $3''$  to  $20''$  from the source; first panel of Fig. 2), except for the edges of the B condensation (knots B1 and B3), where the velocities are lower ( $\sim 150$  km s $^{-1}$ ). The velocity of the central knot (B2) is similar to the other knots in the A–D region. The velocity decreases beyond knot E1 (at  $35''$ , with a velocity of  $\sim 200$  km s $^{-1}$ ), reaching values of  $\sim 150$  km s $^{-1}$  for knots E2 to E4 (from  $40''$  to  $50''$ ), and  $\sim 100$  km s $^{-1}$  for knots G (at  $75''$ ). Finally, the velocity increases slightly up to  $\sim 150$  km s $^{-1}$  for knots H to I (from  $90''$  to  $135''$ ). It should be noted that up to knot E3, the direction of the velocity is in general quite close to the jet axis ( $|\Delta\text{P.A.}| \lesssim 10^\circ$ ), while beyond knot E3 some of the knots present a significant velocity component westwards, perpendicularly to the jet axis ( $|\Delta\text{P.A.}| \simeq 30^\circ\text{--}40^\circ$ ), so that the decrease in velocity is still more noticeable for the velocity component along the jet axis.

We have only been able to measure the proper motions of two knots of the counterjet. For knot Z2 (at  $4.5''$  from the source) the velocity is  $\sim 250$  km s $^{-1}$ , similar to that of knot A2 in the jet. However we measured a significantly lower velocity, of  $\sim 70$  km s $^{-1}$ , for knot Z1 (at  $2.5''$ ). We think that this abnormally low value of the velocity, as compared with the values measured for the remaining knots of the jet and the counterjet, is likely caused by contamination by scattered light and might not represent a measure of a true acceleration in the counterjet.

The proper motions measured for the HH 30-N knots are on the average aligned with the direction of the HH 30 jet. However, the values obtained both for the velocity and the position angle, show a dispersion considerably larger than in the knots of the HH 30 jet (see last panel in Fig. 2 and Table 1). This larger dispersion in the measured values can be due to the fact that in the HH 30-N knots the emission is fainter than in the HH 30 jet, but could also be a consequence of the interaction between the head of the jet and its surroundings.

The global proper motion velocity of the HH 30-N structure is  $\sim 120 \text{ km s}^{-1}$  with P.A.  $\simeq 30^\circ$ , similar to the direction of the HH 30 jet, thus supporting the hypothesis that this group of knots corresponds to the head of the HH 30 jet (López et al. 1996). The velocity values for individual knots range from  $\sim 50$  to  $\sim 300 \text{ km s}^{-1}$ . The largest velocity is measured for knot NC, but most of the knots have velocity values of  $\sim 50 \text{ km s}^{-1}$ . It should be noted that NF, that was identified as a HH knot in previous works, appears very circular and compact in our higher quality images presented here (see Fig. 2); since the proper motion is compatible with zero ( $v_t = 34 \pm 30 \text{ km s}^{-1}$ ), we conclude that it is most probably a field star.

### *Comparison with Previous Observations*

López et al. (1996) measure proper motions for knots C/D and E of the HH 30 jet. The directions of the proper motions we measured are roughly consistent with those derived by López et al. (1996). For the HH 30 jet we obtained a similar velocity for knot E. For knot C/D where López et al. (1996) note that they obtain an absurdly large velocity of  $\sim 700 \text{ km s}^{-1}$ , we now obtain a more reasonable value of  $\sim 300 \text{ km s}^{-1}$ . Mundt et al. (1990) report a still lower proper motion velocity of  $\sim 150 \text{ km s}^{-1}$  for knot C (the only knot for which they measure the proper motion), but since they use images of two epochs obtained through different filters, we think that our value is more reliable. Burrows et al. (1996), from *HST* observations, measure proper motion velocities of  $\sim 100 - 250 \text{ km s}^{-1}$  in the inner  $\sim 5''$  of the jet and velocities of  $\sim 250 \text{ km s}^{-1}$  for distances of  $\lesssim 1''$  in the counterjet. These values are roughly in agreement with the velocities we measured for knots A2, A3 in the jet and Z2 in the counterjet.

Regarding HH 30-N, the only previous available proper motion measurements are those of López et al. (1996) for knots ND, NE, and NF. Our results confirm that the direction of the proper motion velocities of HH 30-N is consistent with HH 30-N belonging to the HH 30 jet, thus supporting the claim of López et al. (1996). However, we obtained significantly lower values for the velocities. In particular, we conclude that knot NF is a field star (see discussion above). Since the knots of HH 30-N are weak and diffuse, we attribute these discrepancies to the lower sensitivity and angular resolution of the images used by López et al. (1996).

In order to better illustrate the comparison with previous observations of the positions and proper motions of the HH 30 jet knots, we plotted in Figure 3 their positions as a function of time. The vertical axis is the distance along the jet, at a position angle of  $30.6^\circ$ . The five vertical lines of each panel mark the epoch of different observations and the circles indicate the position of the knots. Knots are labeled with the last two digits of the year of the observation, followed by the name used by each author. The vertical line with knots

labeled “87” corresponds to the observation carried out in 1987 January by Mundt et al. (1990). Knots labeled “93” correspond to the observation carried out in 1993 December by López et al. (1995). Knots labeled “95” were observed with the Hubble Space Telescope in 1995 January by Burrows et al. (1996). *HST* observations carried out in 1994 February and 1995 March reported in Burrows et al. (1996) and Ray et al. (1996) have not been included for clarity of the figure. The two vertical lines labeled “98” and “99” correspond to the present observations with the NOT telescope. The dotted lines indicate the proper motions of the knots, as measured from the 1998 and 1999 observations, taken from Table 1. The shaded area along the proper motion line of knot 99-C indicates the formal uncertainty of the proper motion measurement for this knot, as it propagates with time. The uncertainties for other knots are similar to this case, shown here as an example. We have not included the data of the observations described in López et al. (1996), observed in 1995 February since they are of much lower quality.

The extrapolation of the proper motions measured from our NOT 1998-1999 data to the epoch of the previous observations intersects the vertical lines at points that, in general, are in agreement with the positions of observed knots. However, this correspondence is better for knots located farther away from the exciting source, while for knots closer to the source the correspondence is more complex. As the right panel of Figure 3 illustrates, a backward extrapolation of our proper motion measurements for knots E1-E4 and G1-G2 (at distances of  $\sim 30''$  to  $\sim 70''$  from the source) provides a good agreement with the positions of the knots E and G actually observed in both the 1987 and 1993 images. The extrapolated position of knot 99-D1 falls very close to the position of knot 95-14N in the *HST* image, while the extrapolated position of knot 99-D2 falls outside the region where the *HST* observations are sensitive enough to detect the jet emission. In the 1993 image, the extrapolation of the proper motions of knots 99-D1 and 99-D2 falls in a region where it is difficult to separate the emission into several knots, and it is designated as 93-D1, while the D2 knot in the 1993 image would probably be displaced too far away (and, thus, too faint) in the 1998-1999 images to be detected. Interestingly, our proper motion extrapolation suggests that knots D (at  $\sim 18''$  from the source) in the 1998-1999 images arise from knot C (at  $\sim 14''$  from the source) in the 1987 image, while knots D in that image would have faded away in our 1998-1999 images. Knot C in our 1998-99 images appears to correspond to knot 93-C, and perhaps to knot 95-13N. For knots B1–B3 in the 1998-1999 images, the extrapolation suggests a correspondence with knots 11N and 12N in the 1995 image, and knots B1 and B2 in the 1987 image. As we noted previously, we derived abnormally low values for the proper motions of knots 99-B1 and 99-B3; an extrapolation of their positions using the proper motion value obtained for B2 would result in a one-to-one correspondence between knots 99-B1, 99-B2 and 99-B3 with knots 95-10N, 95-11N, and 95-12N, respectively. Also, within

current uncertainties, knot 87-B2 could correspond either to the extrapolation of knot 99-C or knot 99-B3.

For knots within  $5''$  from the source, the *HST* image provides much more detail than our ground based 1998-99 images, thus making less useful the backward extrapolation of the NOT proper motions, since each 98 and 99 knot corresponds to more than one 95 knot. However, from the inspection of Figure 3, and using the proper motions reported in Burrows et al. (1996), it is clear that at least some of the 1995 *HST* knots do appear to correspond to structures observed in our ground based images. For example, both the proper motion velocity of  $170 \text{ km s}^{-1}$  reported by Burrows et al. (1996) for knot 95-06N + 95-07N, and our proper motion velocity of  $213 \pm 43 \text{ km s}^{-1}$  obtained for knot 99-A3, suggests that their extrapolated positions coincide. Also the proper motion velocity of  $260 \text{ km s}^{-1}$  reported for knot 95-02N, leads its extrapolated position to coincide with that of knot 99-A2, for which we obtained the same value of the proper motion velocity. Knot 99-A1, which only appears in our 1999 NOT image, had probably still not emerged at the epoch of the *HST* observations. The extrapolated position for the counterjet knot 95-02S with a proper motion velocity of  $280 \text{ km s}^{-1}$  reported by Burrows et al. (1996) appears to correspond with the position of knot 99-Z2, while it is not clear if knot 95-01S corresponds to knot 99-Z1, given its proximity to the source that makes difficult its proper identification in our NOT images.

Globally, it seems that near the source the interaction of the knots with the medium is stronger, and fading out is more important, and thus the changes in intensity and shape of structure makes more difficult the cross-identifications of knots in different epochs.

### 3.2.2. Radial Velocity

Since close to the HH 30 star the [SII] emission of the jet is stronger than the  $\text{H}\alpha$  emission, being also less contaminated by the emission of the star, the heliocentric radial velocities along the HH 30 jet have been derived from the [SII] line profiles. The [SII] 6717, 6731 Å spectra were averaged over regions comparable to the size of the knots and the heliocentric radial velocities obtained for each averaged region (from knot F3 to I1) are listed in Table 2 and shown in Figure 4a. The lines are unresolved with our spectral resolution of  $32 \text{ km s}^{-1}$ . The heliocentric velocity for the region within  $40''$  of the source (knots F3 to E2+E3) remains almost constant, with a value of  $\sim 16 \text{ km s}^{-1}$ , similar to that of the surrounding cloud ( $19 \text{ km s}^{-1}$ ; see Mundt et al. 1990). The heliocentric velocity increases with distance from  $16 \text{ km s}^{-1}$  at  $40''$  (knots E2+E3) to  $47 \text{ km s}^{-1}$  at  $125''$  from the source (knot I1), defining a radial velocity gradient of  $\sim 0.4 \text{ km s}^{-1} \text{ arcsec}^{-1}$  between knots G and I1. These values are consistent with the preliminary results of Raga et al. (1997), although

for the knots close to the source our velocities are  $\sim 10\text{--}15 \text{ km s}^{-1}$  lower. Using a value  $v_t = 200 \text{ km s}^{-1}$  for the proper motions, we derive that the inclination angle,  $\phi$ , of the jet with respect to the plane of the sky ranges from  $4^\circ$  to  $9^\circ$  for distances to the source from  $70''$  to  $120''$ . At smaller distances from the source, the jet lies essentially in the plane of the sky ( $\phi \simeq 0^\circ$ ). Burrows et al. (1996) and Wood et al. (1998), from a fit of the *HST* images to a flared disk using scattered-light models, derive a value of  $\sim 8^\circ$  for the inclination angle of the disk axis with respect to the plane of the sky. However, it should be noted that, although the values obtained for the inclination angle are similar, the derived axis of the jet points away from the observer, while the derived axis of the disk points towards the observer.

Since the [SII] lines are fainter than  $\text{H}\alpha$  in HH 30-N (only knot NC has been detected in [SII]), the radial velocities of HH 30-N have been determined from the  $\text{H}\alpha$  line profiles. After averaging the spectra over regions comparable to the size of the knots, the heliocentric radial velocity and the FWHM for each region were obtained (see Table 3). The velocity dispersion in HH 30-N is much larger than in the HH 30 jet, with values of the FWHM of the lines of typically  $\sim 100 \text{ km s}^{-1}$ . The values obtained for the heliocentric velocity are blueshifted with respect to the ambient cloud, being in agreement with our previous results (Raga et al. 1997). Using a value of  $v_t \simeq 120 \text{ km s}^{-1}$  for the proper motions in HH30-N, we derive that the inclination angle of the jet with respect to the plane of the sky is  $\sim 40^\circ$  (with the jet pointing towards the observer).

In order to study at higher spatial resolution the kinematical pattern we also performed Gaussian fits at different positions inside the knots of HH 30-N. The results are shown in Figure 5, where the heliocentric radial velocity is plotted as a function of projected distance to the HH 30 star. A more detailed inspection of Figure 5 reveals that along knot NA the value of the heliocentric radial velocity progressively decreases (i.e., the absolute value of the velocity relative to the ambient cloud increases) from south to north, with values ranging from  $\sim -70 \text{ km s}^{-1}$  to  $\sim -90 \text{ km s}^{-1}$ . Towards knot NC there is no clear velocity gradient ( $v_{\text{hel}} \simeq -100 \text{ km s}^{-1}$ ), while the velocity increases from  $\sim -100 \text{ km s}^{-1}$  to  $\sim -50 \text{ km s}^{-1}$  from the southern edge of NE to the northern edge of NH. Globally, over the HH 30-N structure, the velocity increases from south to north with an overall gradient of  $0.76 \text{ km s}^{-1} \text{ arcsec}^{-1}$ . The FWHM decreases slightly towards knot NH.

### 3.2.3. Electron Density

In addition to the kinematical information, our spectra also provide information on the electron densities, derived from the [SII] 6717, 6731 Å line ratio. Densities have been obtained assuming a temperature in the [SII] emitting zone of  $10^4 \text{ K}$ . Table 2 and Figure

4b show the electron densities in the knots of the HH 30 jet. A high electron density has been derived for the central region (within a few arcsec of the source), followed by a rapid decrease for the outer knots.

Previous determinations of the electron density in HH 30 (Mundt et al. 1990; Bacciotti et al. 1999) traced only the inner region ( $\sim 10''$ ) of the jet. Our results cover a much more extended region of the jet, up to  $\sim 120''$  from the source. The overall behavior of the electron density, strongly decreasing with distance to the source, agrees with the results of Mundt et al. (1990) and Bacciotti et al. (1999). These authors, with higher angular resolution, measure a strong decrease of electron density from  $\sim 10^4 \text{ cm}^{-3}$  to  $\sim 10^3 \text{ cm}^{-3}$  in the inner  $5''$  of the jet and counterjet; this region approximately corresponds to the region binned for our measurement of  $3.7 \times 10^3 \text{ cm}^{-3}$  at zero position offset. For the region of the jet between  $\sim 5''$  and  $\sim 10''$  from the source, Mundt et al. (1990) give a density of  $\sim 1000 \text{ cm}^{-3}$  while Bacciotti et al. (1999) measure a decrease from  $\sim 1100 \text{ cm}^{-3}$  to  $\sim 370 \text{ cm}^{-3}$ , consistent with our value of  $430 \text{ cm}^{-3}$  measured at  $11''$  from the source. At distances larger than  $\sim 20''$  the density falls to values below  $\sim 100 \text{ cm}^{-3}$ .

In the spectrum of the HH 30-N region the [SII] 6717, 6731 Å emission lines were only detected at knot NC, for which an electron density of  $\sim 380 \text{ cm}^{-3}$  was derived. This increase in the electron density may be produced by the interaction of the jet with an ambient medium of locally enhanced density.

### 3.3. HL/XZ Tau and HH 266

In Table 4 and in Figure 6 we show the proper motion results obtained for the knots near HL/XZ Tau and for HH 266. The nomenclature used for the knots near HL/XZ Tau is consistent with that used by Mundt et al. (1990). These authors consider that knots HL-A and HL-E belong to the HL Tau jet, and HL-B to HL-G belong the HL Tau counterjet. According to Mundt et al. (1990), knots A–D define another jet emanating from a source, VLA 1, with a counterjet defined by knot J. However, the existence of the source VLA 1 is highly doubtful, as shown by more sensitive observations carried out by Rodríguez et al. (1994). Our results for the proper motions show no significant differences in the values of the velocity and position angle for knots HL-A, HL-E, A, B, and D. Thus, our results are consistent with all these knots belonging to the same jet, emanating from HL Tau. Typical values are  $\sim 120 \text{ km s}^{-1}$  for the velocity and  $\sim 45^\circ$  for the P.A., similar to the position angle of the jet axis. Proper motion measurements are more difficult for the knots of the counterjet because many of them are weak and appear split into several subcondensations; in fact, our results are the first determination of proper motions in the HL Tau counterjet.

For all the counterjet knots the proper motion velocities are pointing away from HL Tau. For those with a better determination of their proper motion, HL-C and HL-G, the velocity is  $\sim 120 \text{ km s}^{-1}$ , similar to the values found for the jet knots, and the position angle is  $\sim -110^\circ$ . For knot J we measure a very small proper motion, which does not support the claim of Mundt et al. (1990) that it belongs to the VLA 1 counterjet. Instead, the proper motion of knot J appears to point away from the position of HL Tau as the nearby H $\alpha$ B–C knots do too. Perhaps this group of knots could constitute a low velocity, poorly collimated ejection from HL Tau (at P.A.  $\simeq 170^\circ$ ), although given their very low velocities we do not discard that they constitute a nearly static condensation.

For HH 266 we measured a proper motion velocity of  $\sim 100 \text{ km s}^{-1}$  with a P.A. of  $43^\circ$ . López et al. (1996) note that HH 266 lies at a position that is aligned within only a few degrees with the direction of the HL Tau jet (P.A. =  $45^\circ$ ), suggesting that HH 266 constitutes the head of the HL Tau jet. Our proper motion results give support to this suggestion, since both the position angle of the HH 266 proper motion, which points away from HL Tau, as well as the value of the velocity that is similar to the velocities measured for the knots of the HL Tau jet, give support to this interpretation. However, the uncertainty in the P.A. of the proper motion is not small enough to discard that another object nearby to HL Tau (such as XZ Tau or even the HH 30 star) was the driving source for HH 266.

Mundt et al. (1990) measure proper motions for several knots. In Table 5 we list the values obtained by these authors. As can be seen in the table, the direction of the proper motion velocities we have measured for the HL Tau jet is similar to that found by Mundt et al. (1990). However, the values obtained by these authors are significantly higher than ours. We attribute this discrepancy to the fact that Mundt et al. (1990) derive their proper motions using images obtained with different filters; so, we think that our values are more reliable. In order to obtain an estimate of the proper motions with a longer time baseline, we used the [SII] images published in Mundt et al. (1990) to obtain 1987 epoch positions for several of the knots. By comparing these positions with our NOT 1999 positions we derived proper motions with a time baseline of 12.9 years. The results are given in Table 5. As can be seen in the table, the proper motions obtained in this way are in better agreement with our NOT 1998-1999 measurements.

Since the radial velocity of the HL Tau jet with respect to the ambient cloud is  $\sim -200 \text{ km s}^{-1}$  (Mundt et al. 1990), and proper motions are  $\sim 120 \text{ km s}^{-1}$ , we infer that the total velocity of the HL Tau jet is  $\sim 230 \text{ km s}^{-1}$ , being the angle of the jet with respect to the plane of the sky of  $\sim 60^\circ$  (towards the observer).

The radial velocity of the counterjet measured by Mundt et al. (1990) is  $\sim 100 \text{ km s}^{-1}$ , while the proper motions are similar to those of the jet. This results in a significant difference

of  $\sim 20^\circ$  between the inclination of the jet and the counterjet with respect to the plane of the sky, at scales  $\gtrsim 10''$ . Pyo et al. (2006) also noticed a slight asymmetry of the same sign in the velocities of the jet and the counterjet, resulting in a difference of  $\sim 4^\circ$  between the inclination of the jet and the counterjet, at scales of less than  $2''$

## 4. Discussion on the HH 30 Jet Structure

### 4.1. On the Origin of the Wiggling of the Jet

As noted before, the HH 30 jet presents a wiggling morphology that is particularly evident in the group of knots E1–E4 (see Fig. 2b). If the wiggling was produced as the result of a true helical trajectory of the knots as they move away from the exciting source (e.g., by a deflection, as the jet propagates, because of the encounter with a set of high density clumps), one would expect to see changes in the direction of their proper motions, following a velocity pattern tangent to the helical trajectory (e.g., one would expect knot E1 to move to the right of the jet axis, while knots E2 and E3 to move to the left). Despite the uncertainties in the  $x$  component of the velocities, we do not see evidence for such a systematic pattern; rather, the direction of the proper motion vectors appears to be quite close to that of the axis of the jet. Furthermore, when comparing, for example, the E1–E4 structure in our images with the previous images of Mundt et al. (1990) and López et al. (1995), a displacement can be seen of the whole knot structure, keeping the same morphology, while a change in this morphology would be expected if the knots were following an helical trajectory. This is further illustrated in Figure 3, where it can be seen that the group of knots E1–E4 moves essentially as a whole from one epoch to another, maintaining the same relative distance between knots. Thus, we conclude that the motion of the knots is essentially ballistic and that the observed wiggling of the jet structure is most likely produced by variations in the direction of the ejection at the origin of the jet.

#### 4.1.1. *Orbital Motion of the Jet Source*

We will test the possibility that the observed wiggling in the HH 30 jet results mainly from the orbital motion of the jet source around a binary companion. Following the formulation given by Masciadri & Raga (2002), we will consider a ballistic jet (i.e., a jet where the fluid parcels preserve the velocity with which they are ejected) from a star in a circular orbit, and we will further assume that the ejection velocity (measured in a frame moving with the outflow source) is time independent and parallel to the orbital axis.

Let  $m_1$  be the mass of the jet source,  $m_2$  the mass of the companion, and  $m = m_1 + m_2$  the total mass of the system. We will call  $\mu$  the mass of the companion relative to the total mass, so that

$$\begin{aligned} m_1 &= (1 - \mu) m, \\ m_2 &= \mu m. \end{aligned} \tag{1}$$

Let  $a$  be the binary separation (i.e., the radius of the relative orbit). Therefore, the orbital radius of the jet source with respect to the binary’s center of mass (i.e., the radius of the jet source absolute orbit) is

$$r_o = \mu a, \tag{2}$$

and the orbital velocity of the jet source is given by

$$v_o = \frac{2\pi r_o}{\tau_o}, \tag{3}$$

where  $\tau_o$  is the orbital period.

We will use a Cartesian coordinate system  $(x', y', z')$ , where  $(x', z')$  are in the orbital plane, being the  $x'$  axis the intersection of the orbital plane with the plane of the sky. The  $y'$  axis coincides with the orbital axis, at an angle  $\phi$  with respect to the plane of the sky. The ejection velocity of the jet will have a component in the orbital plane due to the orbital motion,  $v_o$ , and a component perpendicular to this plane,  $v_j$ , assumed to be constant. In this coordinate system the shape of the jet is given by

$$\frac{x'}{r_o} = \kappa \frac{|y'|}{r_o} \sin \left( \kappa \frac{|y'|}{r_o} - \psi \right) + \cos \left( \kappa \frac{|y'|}{r_o} - \psi \right), \tag{4}$$

where  $\kappa \equiv v_o/v_j$ , and  $\psi$  is the orbital phase angle (with respect to the  $x'$  axis) at the epoch of observation. The equation for the  $z'$  coordinate is obtained by substituting  $\psi$  by  $\psi + \pi/2$  in Eq. 4. Note that the jet ( $y' > 0$ ) and counterjet ( $y' < 0$ ) shapes will have a reflection symmetry with respect to the orbital plane.

If  $D$  is the distance from the source to the observer, the positions  $(x, y)$  measured on the observed images (i.e., in the plane of the sky) are given by

$$\begin{aligned} x &= \frac{x'}{D}, \\ y &= \frac{y' \cos \phi - z' \sin \phi}{D} \simeq \frac{y' \cos \phi}{D}, \end{aligned} \tag{5}$$

the last approximation being valid for a collimated jet with a small inclination  $\phi$  at distances large enough from the source ( $y' \gg z'$ ). The parameters of the model are directly related to

the observables:  $\kappa$  is related to the half-opening angle,  $\alpha$ , of the jet cone measured in the plane of the sky,

$$\kappa = \tan \alpha \cos \phi, \quad (6)$$

and the orbital radius  $r_o$  is related to the observed period  $\lambda_y$  of the wiggles (i.e. the angular distance in the plane of the sky between the positions of two successive maximum elongations),

$$r_o = \frac{\lambda_y \tan \alpha}{2\pi} D. \quad (7)$$

In terms of these parameters, Eq. 4 becomes

$$x = |y| \tan \alpha \sin \left[ \frac{2\pi}{\lambda_y} (|y| - y_0) \right] + \frac{\lambda_y}{2\pi} \tan \alpha \cos \left[ \frac{2\pi}{\lambda_y} (|y| - y_0) \right], \quad (8)$$

where  $y_0 = \lambda_y \psi / 2\pi$  is the offset from the origin, in the plane of the sky, of the knot ejected when the source was at the  $\psi = 0$  position.

Wiggling in the HH 30 jet is most evident in the group of knots B, C, D, and E. Therefore, we used knots A1 to E4 to determine the parameters of the jet, and we found a very good match of the predicted shape with the observed image of the jet for  $\alpha = 1^\circ 43 \pm 0^\circ 12$ ,  $\lambda_y = 16'' \pm 1''$  (corresponding to  $2240 \pm 140$  AU at a distance  $D = 140$  pc), and  $y_0 = 4'' \pm 2''$  (corresponding to  $560 \pm 280$  AU). The result is shown in Figure 7a. If this jet shape is translated to the epoch of the *HST* observations reported by Burrows et al. (1996) it is also consistent with the observed positions of the knots, thus confirming the validity of the fit.

Using Eq. 7 and the values obtained for  $\alpha$  and  $\lambda_y$  we derived an orbital radius  $r_o = 8.9 \pm 0.9$  AU (corresponding to  $0''.064 \pm 0''.006$ ). In addition, the fit allowed us to obtain a more accurate value for the position angle of the axis of the jet, P.A. =  $31^\circ 6$ , in the range of offsets from the source of  $0''$  to  $50''$ .

Since the observed ratio of radial to proper motion velocities in the HH 30 jet is very small (see Tables 1 and 2), we infer that the inclination angle should be also very small,  $\phi \lesssim 5^\circ$  (§ 3.2.2). Then, from the proper motion measurements (Table 1) we obtained an estimate of the ejection velocity,  $v_j = v_t / \cos \phi \simeq 200 \pm 50$  km s<sup>-1</sup>, and we derived the remaining orbital parameters. Using Eq. 6 we obtained the orbital velocity,  $v_o = 5.0 \pm 1.3$  km s<sup>-1</sup>, and using Eq. 3 we obtained the orbital period,  $\tau_o = 53 \pm 15$  yr. The line-of-sight component of the orbital velocity will produce an oscillation of the radial velocity along the path of the jet with a peak-to-peak amplitude of  $2v_o \cos \phi \simeq 10.0$  km s<sup>-1</sup>. This value is small compared to the spectral resolution of our observations ( $\sim 32$  km s<sup>-1</sup>), so it is not expected to produce significant oscillations in the observed radial velocity, consistent with what is observed (see Table 2 and Fig. 4). In the case of the HH 43 jet, noticeable radial velocity oscillations

with a peak-to-peak amplitude of  $16 \text{ km s}^{-1}$  were observed with higher spectral resolution by Schwartz & Greene (1999).

The total mass of the binary system is given by

$$\left(\frac{m}{M_{\odot}}\right) = \mu^{-3} \left(\frac{r_o}{\text{AU}}\right)^3 \left(\frac{\tau_o}{\text{yr}}\right)^{-2}, \quad (9)$$

corresponding to  $m = 0.25 \mu^{-3} M_{\odot}$ , for the values of  $r_o$  and  $\tau_o$  derived above. For a system with two stars of the same mass ( $\mu = 0.5$ ), each component will have a mass of  $1.0 \pm 0.3 M_{\odot}$ , and the separation between the two components would be  $a = r_o/\mu = 17.8 \text{ AU}$  ( $0''.128$ ). Values of  $\mu < 0.5$  (corresponding to the jet source being the primary) would result in  $m > 2 M_{\odot}$ , and appear unlikely, given the estimated low bolometric luminosity of the system ( $L \simeq 0.2\text{--}0.9 L_{\odot}$  that, according to D’Antona & Mazzitelli 1997 would correspond to stellar masses roughly in the range  $0.1\text{--}1 M_{\odot}$ ). Smaller masses would be obtained if  $\mu > 0.5$  (corresponding to the jet source being the secondary), with a lower limit of  $m_2 = 0.25 M_{\odot}$  ( $\mu = 1$ ), and a separation  $a = r_o$ . Thus, under this scenario we expect that the exciting source of the HH 30 jet belongs to a close binary system, with the two components separated by  $0''.064\text{--}0''.128$ , and the total mass of the system in the range  $0.25\text{--}2 M_{\odot}$ .

#### 4.1.2. Precession of the Jet Axis

An alternative possibility is that the observed wiggling of the HH 30 jet is due to precession of the ejection axis of the jet, being driven by tidal interactions between the disk from which the jet originates and a companion star in a non coplanar orbit. For this model we will neglect the orbital motion of the jet source, and we will assume that the wiggling of the jet is the result of the changing direction of ejection of the jet. Masciadri & Raga (2002) show that the shape of the jet is given by

$$x' = y' \tan \beta \cos \left( \frac{2\pi}{\tau_p} \frac{|y'|}{v_j \cos \beta} - \psi \right), \quad (10)$$

where  $\beta$  is the angle between the central flow axis and the line of maximum deviation of the flow from this axis, and  $\tau_p$  is the precession period. Note that in this case the jet ( $y' > 0$ ) and counterjet ( $y' < 0$ ) shapes will have a point symmetry with respect to the jet source.

The precession angle,  $\beta$ , is related to the observables  $\alpha$  (the half-opening angle of the jet cone measured in the plane of the sky) and  $\phi$  (the inclination angle of the jet axis with respect to the plane of the sky) as,

$$\tan \beta = \tan \alpha \cos \phi, \quad (11)$$

and the precession period  $\tau_p$  is related to  $\lambda_y$  (the observed angular period of the wiggles) and  $v_t$  (the measured proper motion velocity, where  $v_t = v_j \cos \phi$ ) as,

$$\tau_p = \frac{\lambda_y D}{\tau_p v_t \cos \beta}. \quad (12)$$

Therefore, Eq. 10 can be rewritten in angular coordinates in the plane of the sky and in terms of observable parameters as,

$$x = y \tan \alpha \cos \left[ \frac{2\pi}{\lambda_y} (|y| - y_0) \right]. \quad (13)$$

An approximate expression relating the orbital and precession periods can be derived from Eq. 24 of Terquem (1998), valid for a disk precessing as a rigid body, by assuming that the disk surface density is uniform and that the rotation is Keplerian,

$$\frac{\tau_o}{\tau_p} = \frac{15}{32} \frac{\mu}{(1 - \mu)^{1/2}} \sigma^{3/2} \cos \beta, \quad (14)$$

where  $\mu = m_2/m$  is the ratio between the mass of the companion and the total mass of the system,  $\beta$  is the inclination of the orbital plane with respect to the plane of the disk (coincident with half the opening angle of the precession cone), and  $\sigma = r_d/a$  is the ratio of disk radius to binary separation.

From the fit to the observed shape of the jet for knots A–E we obtained the values of  $\alpha$  and  $\lambda_y$  (§ 4.1.1), and using Eqs. 11 and 12 we obtain a precession angle  $\beta = 1^\circ 42 \pm 0^\circ 12$  and a precession period  $\tau_p = 53 \pm 15$  yr, for  $v_j = 200$  km s<sup>-1</sup> (§ 4.1.1). The expected peak-to-peak oscillation of the observed radial velocity corresponding to this precession motion is  $2 v_j \sin \beta \cos \phi = 9.9$  km s<sup>-1</sup>, a value similar to that expected in the case of pure orbital motion, and that is too small to be detectable, given the spectral resolution of our observations. Unlike the case of orbital motion, in the case of precession, the observables do not tightly constrain the orbital parameters, and a number of additional assumptions are required to infer their values. Since it is expected that the size of the disk is truncated by tidal interaction with the companion star in such a way that  $1/4 \leq \sigma \leq 1/2$  (Lin & Papaloizou 1993; Artymowicz & Lubow 1994; Larwood et al. 1996; Terquem et al. 1999), we will adopt a value of  $\sigma = 1/3$ , so that using Eq. 14 the orbital period can be obtained from the observables as a function of only the parameter  $\mu$ . An additional constraint comes from the observed luminosity of the source that, according to D’Antona & Mazzitelli (1997), suggests that the mass of the more massive of the two components should fall in the range 0.1–1  $M_\odot$ . Finally, the hypothesis that the observed wiggling in the jet is mainly due to precession implies that the effect on the jet opening angle produced by the orbital motion

of the jet source should be smaller than the precession angle ( $v_o/v_j < \tan \beta$ ). According to Eq. 6, the orbital velocity of the jet source should be  $v_o < 5 \text{ km s}^{-1}$  in order to fulfill this condition.

Taking into account these constraints, we investigated the parameter space for different values of  $\mu$ . For a given value of  $\mu$  we calculated the orbital period using Eq. 14. Then, for each value of  $v_o$  we derived the value for  $r_o$  by using Eq. 3, and using Eq. 2 the corresponding separation between the two stars. The mass of the binary system was calculated using Eq. 9, and the corresponding masses of the two components were calculated using Eq. 1. Following this procedure we found that the orbital velocity and luminosity constraints lead to the result that the more massive of the two components (with a mass between  $0.1$  and  $1 M_\odot$ ) should be the jet source. The maximum orbital velocity of  $5 \text{ km s}^{-1}$  gives the largest values of the mass of the companion ( $m_2 = 0.17 M_\odot$ ). Specifically, for  $v_o = 5 \text{ km s}^{-1}$ , the mass of the jet source should be in the range  $0.1 < m_1 < 1 M_\odot$ , resulting in a mass of the companion  $0.07 < m_2 < 0.17 M_\odot$ , a binary separation  $1.04 > a > 0.86 \text{ AU}$  (corresponding to an angular separation between  $0''.007$  and  $0''.006$ ), and an orbital period  $2.5 > \tau_o > 0.8 \text{ yr}$ , respectively. The actual value of the orbital velocity should be significantly lower than  $5 \text{ km s}^{-1}$ , resulting in very low values for the mass of the companion and the binary separation. For instance, for  $v_o = 2 \text{ km s}^{-1}$ , the mass of the companion is  $0.01 < m_2 < 0.04 M_\odot$ , the binary separation is  $a = 0.33 \text{ AU}$  ( $0''.002$ ), and the orbital period is  $0.6 > \tau_o > 0.2 \text{ yr}$ . Therefore, in the precession scenario the companion is expected to be a brown dwarf star or even a giant exoplanet.

#### 4.1.3. Evidence for a Binary Exciting Source

After the discussion in the previous section we conclude that both the orbital motion and the precession models are feasible. In the first case, the orbital period would be  $53 \text{ yr}$ , the expected angular separation would be  $0''.064\text{--}0''.128$  ( $9\text{--}18 \text{ AU}$ ), and the jet source is expected to be the secondary, while the mass of the primary is expected to fall in the range  $0.25\text{--}1 M_\odot$ . In the case of precession, in order to fulfill the observational constraints, the jet source should be the primary, with a mass in the range  $\sim 0.1\text{--}1 M_\odot$ , resulting in much smaller values for the derived parameters: the orbital period is expected to be less than  $\sim 1 \text{ yr}$ , the mass of the companion less than a few times  $\sim 0.01 M_\odot$ , and the angular separation  $< 0''.007$  ( $< 1 \text{ AU}$ ).

We want to emphasize that both scenarios are consistent with the current observational data, and that both imply that the exciting source of the HH 30 jet should be a close binary (separation  $< 0''.1$ ). We take the very good agreement between the predicted and observed wiggling of the HH 30 jet as a strong (although indirect) evidence for the existence of such a

binary system. A direct evidence would require to resolve the HH 30 exciting source with an angular resolution better than  $\sim 0''.1$  in the case of orbital motions and better than  $\sim 0''.01$  in the case that the wiggling is originated by precession. Given the strong extinction towards the source and the high angular resolution required, observations at centimeter, millimeter, or submillimeter wavelengths will be necessary. In the first scenario, the required angular resolution can be currently achieved with the VLA although, unfortunately, the source appears to be weak at centimeter wavelengths, and has not been detected yet (Carrasco-González et al. 2007). In the precession scenario, the angular resolution required is near the limits of the expected capabilities of ALMA.

In both scenarios the range of values inferred for the mass of the system is consistent with the estimate for the stellar mass of  $0.45 \pm 0.04 M_{\odot}$  obtained from IRAM Plateau de Bure  $^{13}\text{CO}$  observations of the disk (Pety et al. 2006). We also note that Stapelfeldt et al. (1999) find variability in the asymmetry of the disk suggesting a characteristic time scale of 3 yr or less, which is of the order of the values of the orbital period derived in the precession scenario. This coincidence should be expected if the variability of the illumination pattern were produced by an eclipsing binary system with this orbital period.

The two proposed scenarios could be discriminated by taking into account that in the first case mirror symmetry between the jet and counterjet is expected, while in the second case point symmetry is expected to be found. Unfortunately, our images do not cover the counterjet and we cannot discriminate between both possibilities. We expect that future observations will allow us to discriminate between the two scenarios.

We also note that, in both scenarios, the expected separation between the two components of the binary system is  $< 18$  AU, a value much smaller than the radius of the disk nearly perpendicular to the HH 30 jet observed with the *HST* (Burrows et al. 1996, Stapelfeldt et al. 1999), which is  $\sim 250$  AU. Given that the radius of any circumstellar disk associated with the jet source should be smaller than the binary separation, this implies that the *HST* disk should be a circumbinary disk and not a circumstellar disk. Also, since the scale of the jet collimating mechanism should be much smaller than that of the mechanism that drives the jet wiggling, which is of the order of the binary separation ( $< 18$  AU), we conclude that the  $\sim 250$  AU disk observed with the *HST* is unlikely to have a relevant role in the jet collimation, contrary to what has been thought up to now. These results suggest that the search for the true collimating agent of the HH 30 jet (likely a circumstellar disk associated with the jet source) should be done at very small angular scales,  $< 0''.13$  ( $< 18$  AU).

## 4.2. The Large-Scale Structure of the HH 30 Jet

As a general trend, we observe that the direction of the proper motions measured for the knots of the HH 30 jet approximately coincides with that of the geometrical axis of the jet (see Fig. 2 and Table 1). There is, however, some indication of a systematic velocity component perpendicular to the axis of the jet, so that the resulting proper motion velocities deviate to the right of the jet axis (i.e., the velocities are orientated at a P.A. that, in general, is smaller than that of the jet axis, whose P.A. is  $\sim 30^\circ$ ). The presence of this velocity component perpendicular to the jet axis is in agreement with the suggestion of López et al. (1995) that the observed “axial rotation” effect in the HH 30 jet (i.e., the direction of the axis of the jet and counterjet curves westward as one moves away from the exciting source) is a consequence of the relative motion between the source and the environment. Such a scenario has been modeled in detail by Cantó & Raga (1995). The proximity of the powerful L1551-IRS5 molecular outflow, to the southeast of the HH 30 jet, could also contribute to the velocity component perpendicular to the jet axis.

The wiggling-model fit obtained for the jet at distances smaller than  $\sim 50''$  (see § 4.1) is also essentially valid for larger scales. In Figures 1 and 7b we show the resulting structure of the jet up to distances of  $\sim 300''$ . In this fit we introduced a slight change of  $-5^\circ$  in the P.A., at a distance of  $72''$  from the source, in order to reproduce the bending of the jet (see discussion above). As can be seen in the Figure, in this way the overall structure of the jet is reproduced quite well, including the width of the jet up to the distance of HH 30-N. We take this as an additional proof that the HH 30-N knots do belong to the HH 30 jet (and that HH 266 does not belong to the HH 30 jet). Also, we take this good agreement as additional evidence for the presence of a binary system in the exciting source of the HH 30 jet.

We note that the detailed oscillations of the jet are not well reproduced for distances higher than  $\sim 50''$ . This can be due to slight variations in the ejection velocity (in fact, proper motions are not constant) that would result in increasingly larger deviations of the periodic pattern as the distance from the source increases. In fact, a change in the radial velocity is observed at a distance of  $\sim 70''$  from the source, coinciding with the  $\Delta\text{P.A.} = -5^\circ$  of the jet.

Finally, we point out that if one wants to explain the knot/inter-knot pattern of the HH 30 jet as the result of source variability with a multiple mode model (as derived by Raga & Noriega-Crespo 1998 for the HH 34 jet), we would need at least four modes. One of these modes would have a  $\tau_1 \simeq 2.5$  yr period, as derived by Burrows et al. (1996) for the *HST* knots 02–04N. We would then need a second  $\tau_2 \simeq 30$ –40 yr period to explain the separation between features such as the knot that corresponds to the *HST* knots 06+07N and the condensation composed by the *HST* knots 02–04N (see Fig. 3). A similar period

is found from the velocities and separation between knots B and C, and knots E1 and E2 (see Figs. 2 and 3). A third,  $\tau_3 \simeq 150$  yr period is necessary to produce the separations between knots B/C, E, G and H. Finally, in order to produce the NA-NH knot structure (see Figs. 1 and 2), one would need a fourth source variability mode. The dynamical timescale  $\tau_{\text{dyn}} \simeq 1500$  yr  $\simeq \tau_4$  of the NA–NH knots indicates the order of magnitude of the period of this fourth mode.

Even though there is little doubt that the *HST* knot spacing pattern is generated very close to the outflow source (see Burrows et al. 1996), it is clearly possible that the larger scale knot patterns could originate at larger distances from the source (e. g., through instabilities developed along the jet beam). The question of whether or not these larger scale knot patterns are also generated as a consequence of source variability should be settled in the future through high angular resolution monitoring of the HH 30 jet during the following  $\sim 30$  years.

## 5. Conclusions

Using the NOT we obtained [S II] CCD frames at two epochs with a time span of one year of the region enclosing HH 30, HH 30-N, HH 266, as well as HL/XZ Tau. We also obtained high-resolution optical spectroscopy of the HH 30 jet (including HH 30-N) using the WHT. The main conclusions from the analysis of our results can be summarized as follows:

1. We measured proper motions in the HH 30 jet, with velocities ranging from  $\sim 100$  to  $\sim 300$  km s $^{-1}$ . We found the highest values of the velocity (200–300 km s $^{-1}$ ) near the driving source ( $< 3000$  AU), decreasing to  $\sim 150$  km s $^{-1}$  at distances of  $\gtrsim 5000$  AU.
2. Although the jet shows a wiggling morphology, the proper motions of the jet knots are roughly parallel to the jet axis, with no signs of a pattern of changes in the direction as would be expected for a true helical motion of the knots. This suggests that the motion of the knots is essentially ballistic and that the observed wiggling is most likely produced by variations in the direction of the velocity at the origin of the jet. Nevertheless, there is a small but systematic drift of the velocities westwards, which could be due to the effect of a side wind.
3. We have been able to measure reliable proper motions only for one of the knots of the counterjet, obtaining a velocity of  $\sim 250$  km s $^{-1}$ , which is similar to the velocities measured in the jet at similar distances.

4. The proper motions measured for the HH 30-N knots are, on the average, aligned with the direction of the HH 30 jet, thus supporting the hypothesis that this group of knots corresponds to the head of the HH 30 jet (López et al. 1996). However, the values obtained for both magnitude and position angle of the velocity show a dispersion considerably larger than in the HH 30 jet, which could be a consequence of the interaction between the head of the jet and its surroundings.

Knot NF, which was previously identified as a HH knot, appears very circular and compact in our higher quality images, and with a proper motion compatible with being static. We thus conclude that it is most probably a field star.

5. The values we obtained for the proper motions along the HH 30 jet are similar to those derived from *HST* data by Burrows et al. (1996) for the inner ( $< 5''$ ) region of the jet. We found a good agreement between the direction of our proper motions and that obtained by López et al. (1996), although we found discrepancies with the values of the velocity derived by these authors (and by Mundt et al. 1990) that we attribute to the poorer quality of their data.
6. In general, we found a pretty good correspondence between the extrapolation back in time of our proper motion estimates for the HH 30 knots and the positions of the knots identified in previous observations. This result indicates that most of the knots probably consist of persisting outflowing structures. However, in some parts of the jet, particularly near the source ( $\lesssim 20''$ ), where the interaction of the jet with the medium appears to be stronger and fading is more noticeable than at larger distances, the knot structure shows indications for an additional static pattern, that could arise from the interaction with the ambient cloud.
7. Our spectroscopic observations show that the radial velocity of the jet is similar to the systemic velocity of the cloud. From the ratio of the radial to proper motion velocities we inferred that the jet lies essentially in the plane of the sky ( $\phi \simeq 0^\circ$ ) for distances to the source  $< 40''$ . For distances to the source  $70'' < y < 120''$  the jet is redshifted with respect to the ambient cloud, with an inclination angle with respect to the plane of the sky  $4^\circ < \phi < 9^\circ$ . For the HH 30-N structure, the radial velocity is blueshifted with respect to the ambient cloud, with an inclination angle with respect to the plane of the sky  $\phi \simeq 40^\circ$ , suggesting a bending of the direction of the jet propagation, as previously proposed by Raga et al. (1997).
8. We estimated the electron density of the HH 30 jet knots up to  $\sim 120''$  from the source, and in HH 30-N, covering a region much more extended than in previous studies. The density in the HH 30 jet decreases with distance to the source, remaining

below  $\sim 100 \text{ cm}^{-3}$  for distances  $\sim 20''\text{--}\sim 120''$ . The density increases to  $\sim 400 \text{ cm}^{-3}$  in HH 30-N, suggesting an interaction of the jet with an ambient medium of locally enhanced density.

9. Our images reveal a clear wiggling of the HH 30 jet knots, with a spatial periodicity of  $16'' \pm 1''$  ( $2240 \pm 140 \text{ AU}$ ). The width of the jet beam increases with distance to the source, with a half-opening angle in the plane of the sky of  $1^\circ 43 \pm 0^\circ 12$ . We found that the wiggling structure of the HH 30 can be accounted for either by the orbital motion of the jet source or by the precession of the jet axis.

In the first case the orbital period of the binary system would be 53 yr, the expected angular separation of the two components would be  $0''.064\text{--}0''.128$  (9–18 AU), and the jet source is expected to be the secondary, while the mass of the primary is expected to fall in the range  $0.25\text{--}1 M_\odot$ . In the case of precession the jet source should be the primary, with a mass in the range  $\sim 0.1\text{--}1 M_\odot$ . The orbital period should be less than 1 yr, the mass of the companion less than a few times  $0.01 M_\odot$ , and the angular separation  $< 0''.007$  ( $< 1 \text{ AU}$ ). Therefore, it is feasible that the secondary is a substellar object, or even a giant exoplanet.

10. We take the very good agreement between the predicted and observed wiggling of the HH 30 jet as a strong (although indirect) evidence for the existence of a binary system. The angular separation between the two components is very small ( $\lesssim 0''.1$  in the case of orbital motion and  $\lesssim 0''.01$  in the case of precession), and would require the use of VLA or ALMA to resolve the system.

In either case, the separation between the two components of the binary is well below the size ( $\sim 450 \text{ AU}$ ) of the observed disk perpendicular to the jet, indicating that this disk should be a circumbinary disk instead of a circumstellar disk, contrary to what has been thought up to now. This leaves unclear the role of the observed disk in the jet collimation, suggesting that the search for a circumstellar disk (likely the true collimating agent of the HH 30 jet) should be carried out at very small scales ( $< 0''.1$ ).

11. Our fit of the observed knot structure of the jet allowed us to refine the value of the position angle of the axis of the jet, obtaining a value of P.A. =  $31^\circ 6$ . In fitting the large scale structure (up to  $300''$ ) we need to introduce a change in the direction of the jet,  $\Delta \text{P.A.} = -5^\circ$  at a distance  $\sim 70''$ . This change in the direction occurs roughly at the same position where there is a change in the radial velocities observed, suggesting a change in the inclination angle with respect to the plane of the sky.
12. We obtained a more accurate estimate of the proper motions of the HL Tau jet, which are of the order of  $\sim 120 \text{ km s}^{-1}$ , a value significantly lower than previous estimates.

From our proper motions and using the radial velocity measurements of Mundt et al. (1990), we estimated that the inclination angle of the HL Tau jet with respect to the plane of the sky is  $\sim 60^\circ$ . We measured for the first time the proper motions in the HL Tau counterjet, obtaining values similar to those of the jet.

G. A., R. L., R. E., and A. R. are supported by the MEC AYA2005-05823-C03 grant (co-funded with FEDER funds). G.A. and J.M. acknowledge support from Junta de Andalucía. The work of A. C. R. was supported by the CONACyT. We thank Luis F. Miranda for his valuable comments and his help in preparing Figure 1. We thank an anonymous referee for helpful comments. The data presented here were taken using ALFOSC, which is owned by the Instituto de Astrofísica de Andalucía (IAA) and operated at the Nordic Optical Telescope under agreement between the IAA and the NBIfA of the Astronomical Observatory of Copenhagen.

## REFERENCES

- Artymowicz, P., & Lubow, S. H. 1994, *ApJ*, 421, 651
- Bacciotti, F., Eisloffel, J., & Ray, T. P. 1999, *A&A*, 350, 917
- Burrows, C. J., Stapelfeldt, K. R., Watson, A. M., Krist, J. E., Ballester, G. E., Clarke, J. T., Crisp, D., Gallagher, J. S., Criffiths, R. E., Hester, J. J., Hoessel, J. G., Holtzman, J. A., Mould, J. R., Scowen, P. A., Trauger, J. T., & Westphal, J. A., 1996, *ApJ*, 473, 437.
- Calvet, N., Cantó, J., & Rodríguez, L. F. 1983, *ApJ*, 268, 739
- Cantó, J., & Raga, A. C. 1995, *MNRAS*, 277, 1120
- Carrasco-González, C. et al. 2007, in preparation
- Carter, D., Benn, C. R., Rutten, R. G. M., et al. 1994, *WHT ISIS user's Manual*, Isaac Newton Group Telescopes, Royal Greenwich Observatory
- Cohen, M. 1983, *ApJ*, 270, L69
- Cotera, A. S., Whitney, B. A., Young, E., Wolff, M. J., Wood, K., Povich, M., Schneider, G., Rieke, M., & Thompson, R. 2001, *ApJ*, 556, 958
- D'Antona, F., & Mazzitelli, I. 1997, *Memorie della Societa Astronomica Italiana*, 68, 807
- Graham, J. A., & Heyer, M. H. 1990, *PASP*, 102, 972
- Haas, M., Leinert, C., & Zinnecker, H. 1990, *A&A*, 230, L1
- Kenyon, S.J., Dobrzycka, D., & Hartmann, L. 1994, *AJ*, 108, 1872
- Kenyon, S. J., Brown, D. I., Tout, C. A., & Berlind, P. 1998, *AJ*, 115, 2491
- Krist, J. E., Stapelfeldt, K. R., & Burrows, C. J. et al. 1999, *ApJ*, 515, L35
- Larwood, J. D., Nelson, R. P., Papaloizou, J. C. B., & Terquem, C. 1996, *MNRAS*, 282, 597
- Lay, O. P., Carlstrom, J. E., & Hills, R. E. 1997, *ApJ*, 489, 917
- Lay, O. P., Carlstrom, J. E., Hills, R. E., & Phillips, T. G. 1994, *ApJ*, 434, L75
- Lin, D. N. C., & Papaloizou, J. C. B. 1993, *Protostars and Planets III*, 749
- Looney, L. W., Mundy, L. G., & Welch, W. J. 2000, *ApJ*, 529, 477

- López, R., Raga, A. C., Riera, A., Anglada, G., & Estalella, R., 1996, MNRAS, 274, L19.
- López, R., Riera, A., Raga, A. C., Anglada, G., López, J. A., Noriega-Crespo, A., & Estalella, R., 1996, MNRAS, 282, 470.
- Masciadri, E., & Raga, A. C. 2002, ApJ, 568, 733
- Monin, J.-L., Pudritz, R. E., & Lazareff, B. 1996, A&A, 305, 572
- Mundt, R., Brugel, E. W., & Bührke, T., 1987, ApJ, 319, 275.
- Mundt, R., Ray, T. P., & Bührke, T., 1988, ApJ, 333, L69.
- Mundt, R., Ray, T. P., Bührke, T., Raga, A. C., & Solf, J., 1990, A&A, 232, 37.
- Mundt, R., Ray, T. P., & Raga, A. C., 1991, A&A, 252, 740.
- Mundt, R., & Fried, J. W. 1983, ApJ, 274, L83
- Mundy, L. G., Looney, L. W., Erickson, W., Grossman, A., Welch, W. J., Forster, J. R., Wright, M. C. H., Plambeck, R. L., Lugten, J., & Thornton, D. D. 1996, ApJ, 464, L169
- Pety, J., Gueth, F., Guilloteau, S., & Dutrey, A. 2006, A&A, 458, 841
- Pyo, T.-S., Hayashi, M., Kobayashi, N., et al. 2006, ApJ, 649, 836
- Raga, A. C., López, R., Riera, A., Estalella, R., & Anglada, G., 1997, Rev. Mex. Astron. Astrof., 33, 127.
- Raga, A. C., & Noriega-Crespo, A., 1998, AJ, 116, 2943.
- Ray, T. P., Mundt, R., Dyson, J. E., Falle, S. A. E. G., & Raga, A. C. 1996, ApJ, 468, L103
- Reipurth, B., Raga, A. C., & Heathcote, S., 1992, ApJ, 392, 145.
- Rodríguez, L. F., Cantó, J., Torrelles, J. M., Gómez, J. F., Anglada, G., & Ho, P. T. P. 1994, ApJ, 427, L103
- Sargent, A. I., & Beckwith, S. 1987, ApJ, 323, 294
- Sargent, A. I., & Beckwith, S. V. W. 1991, ApJ, 382, L31
- Schwartz, R. D. & Greene, T. P. 1999, AJ, 117, 456

- Stapelfeldt, K. R., Watson, A. M., Krist, J. E., Burrows, C. J., Crisp, D., Ballester, G. E., Clarke, J. T., Evans, R. W., Gallagher, J. S. III, Griffiths, R. E., Hester, J. J., Hoessel, J. G., Holtzman, J. A., Mould, J. R., Scowen, P. A., & Trauger J. T. 1999, *ApJ*, 516, L95
- Terquem, C. E. J. M. L. J. 1998, *ApJ*, 509, 819
- Terquem, C., Eislöffel, J., Papaloizou, J. C. B., & Nelson, R. P. 1999, *ApJ*, 512, L131
- Torrelles, J. M., Anglada, G., Rodríguez, L. F., Cantó, L. F., & Barral, J. F. 1987, *A&A*, 177, 171
- Vrba, F. J., Rydgren, A. E., & Zak, D. S. 1985, *AJ*, 90, 2074
- Welch, W. J., Hartmann, L., Helfer, T., & Briceño, C. 2000, *ApJ*, 540, 362
- Wilner, D. J., Ho, P. T. P., & Rodríguez, L. F. 1996, *ApJ*, 470, L117
- Wood, K., Kenyon, S. J., Whitney, B., & Turnbull, M. 1998, *ApJ*, 497, 404

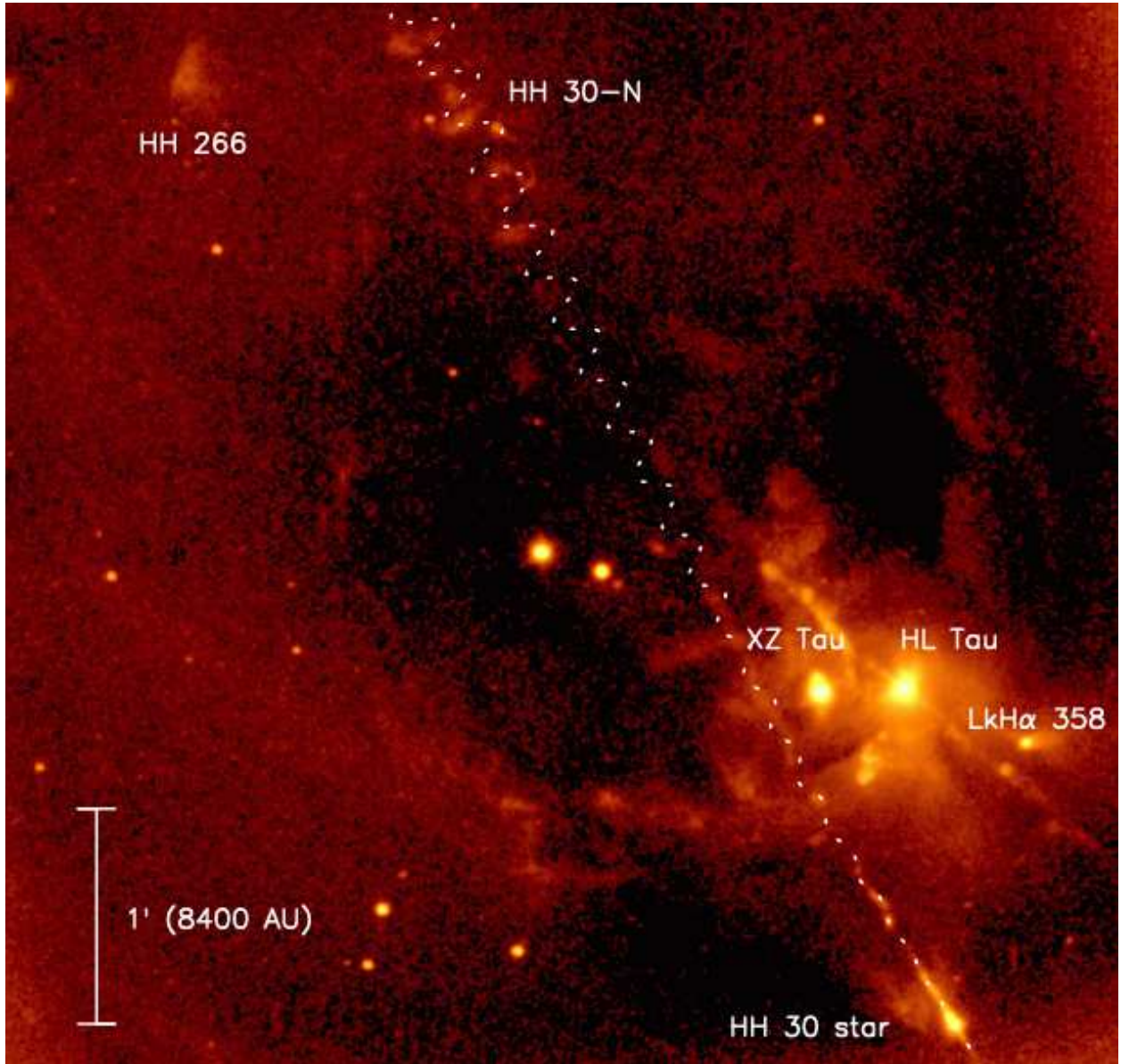


Fig. 1.— NOT 1998 [SII] image of the region surrounding the HH 30 jet, and the HL/XZ Tau stars. North is up and east is to the left. The dotted line is the shape of a wiggling jet model for the HH 30 jet (see text).

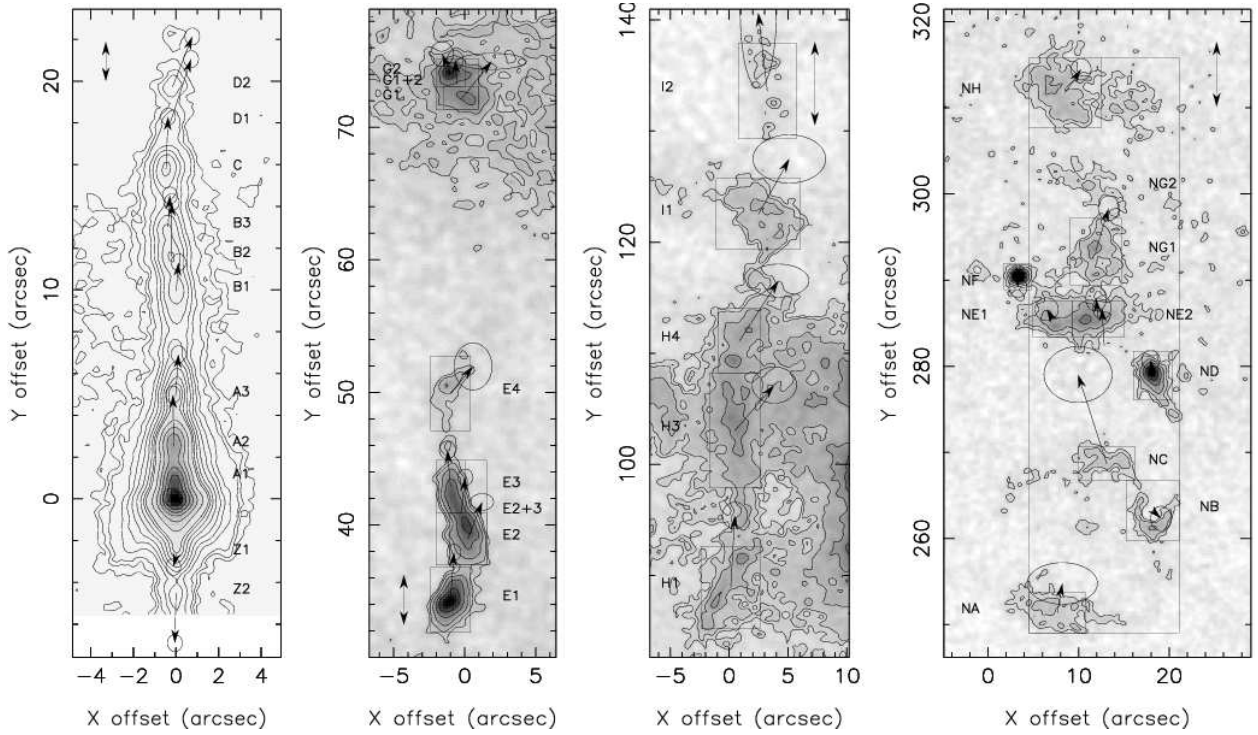


Fig. 2.— Proper motions of the HH 30 jet, shown on the NOT 1999 [SII] image. In (a) we show the knots A to D and the counterjet, in (b) knots E to G, in (c) knots H to I, and in (d) knots N. For knots E to N we also show the box used for calculating the proper motion of each knot. The  $y$  axis, along the jet, is at a position angle of  $30^{\circ}.6$ . Both axes are labeled in arcsec, measured from the position of knot A0 (see Table 1). Arrows indicate the proper motion velocity of each knot. The origin of each arrow is at the peak position of the corresponding knot (A to D), or at the center of the box used for calculating the proper motion (E to N). Ellipses at the end of each arrow indicate the uncertainty in the components of the velocity vector. The scale of the arrows is indicated by the double headed arrow shown in a corner of each map, corresponding to a velocity of  $200 \text{ km s}^{-1}$ .

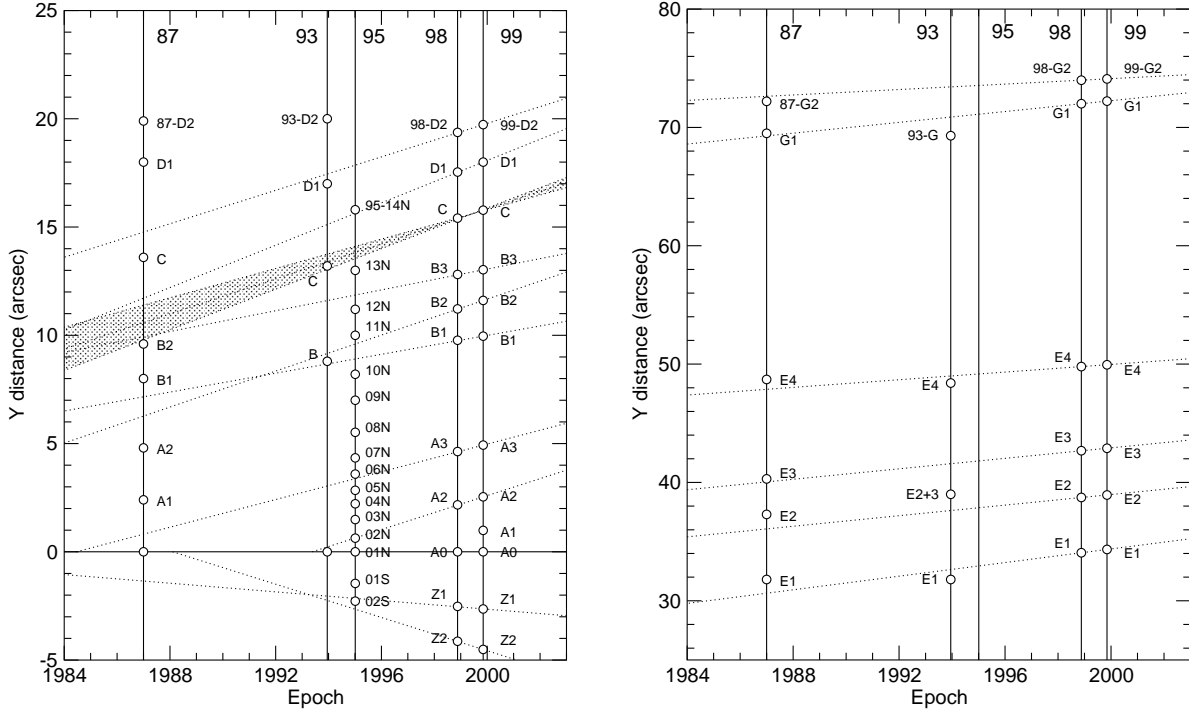


Fig. 3.— Positions of the knots in the HH 30 jet as a function of time. The vertical  $y$  axis is in the direction of the jet axis. The zero of the  $y$  axis has been set to the position of the brightest knot in the ground-based observations, A0, which we identified with knot 95-01N in the *HST* image. Three vertical lines of each panel mark the epoch of previous observations (87: Mundt et al. 1990; 93: López et al. 1995; 95: Burrows et al. 1996). The two rightmost vertical lines indicate the 1998 and 1999 observations with the NOT telescope (this paper), with the dotted lines indicating the extrapolated proper motions of the knots. The shaded area along the proper motion line of knot 99-C indicates the typical uncertainty of the proper motion measurement as it propagates with time. Note that the scale of the  $y$  axis is different in the two panels.

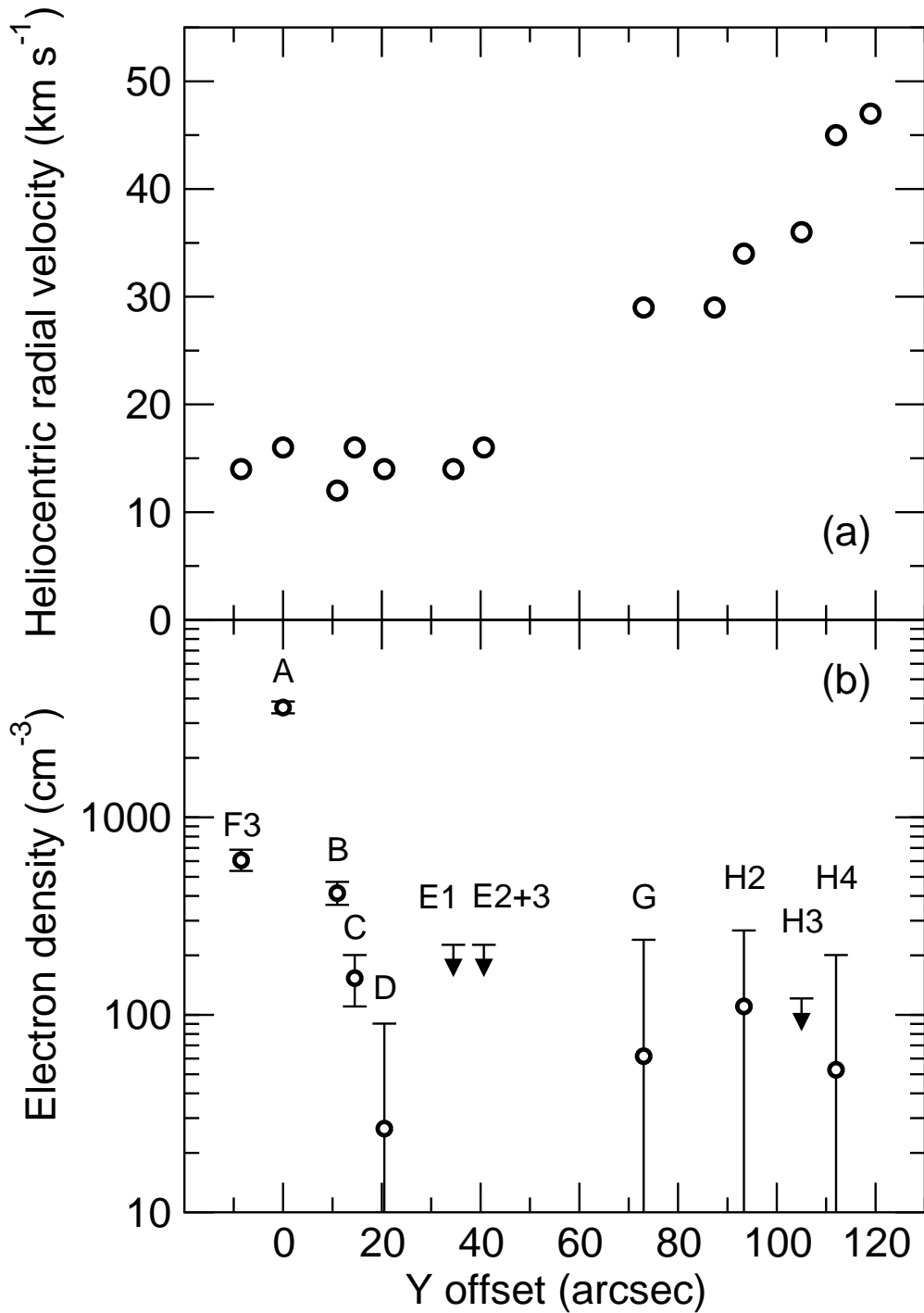


Fig. 4.— [SII] 6717 Å heliocentric radial velocity (a) and electron density (b) of the HH 30 jet knots as a function of distance from knot A0 (see Table 1). The typical velocity uncertainty is  $\sim 5 \text{ km s}^{-1}$ . The heliocentric velocity of the ambient cloud is  $\sim 19 \text{ km s}^{-1}$  (Mundt et al. 1990). Error bars indicate the uncertainty in the derived electron density.

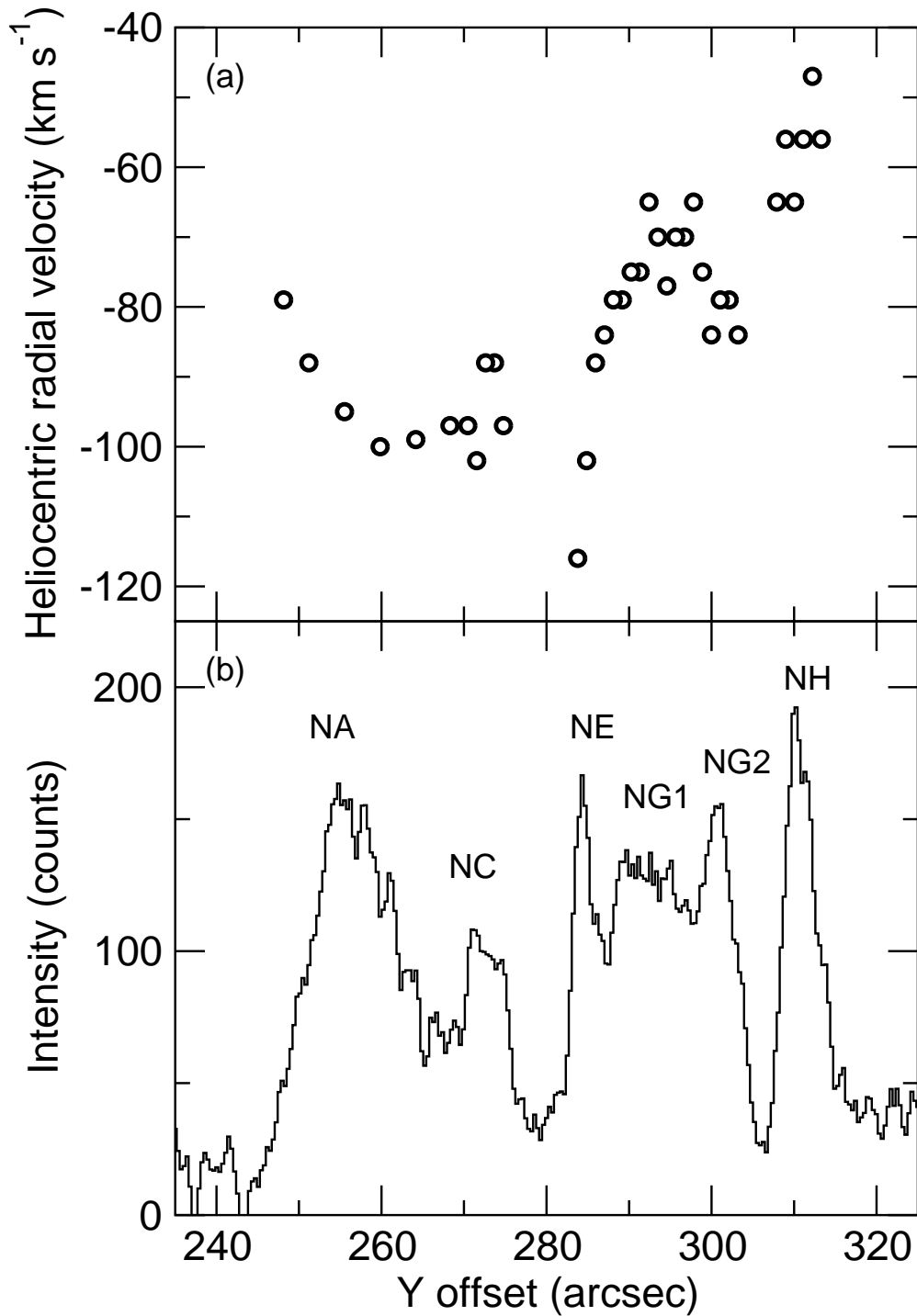


Fig. 5.—  $H\alpha$  heliocentric radial velocities of HH 30-N as a function of distance from knot A0 (see Table 1) (upper panel). The spatial profile along HH 30-N of the  $H\alpha$  emission integrated over the width of the slit, is also plotted to aid in the location of the emission knots (lower panel). The typical velocity uncertainty is  $\sim 5 \text{ km s}^{-1}$ . The heliocentric velocity of the ambient cloud is  $\sim 19 \text{ km s}^{-1}$  (Mundt et al. 1990).

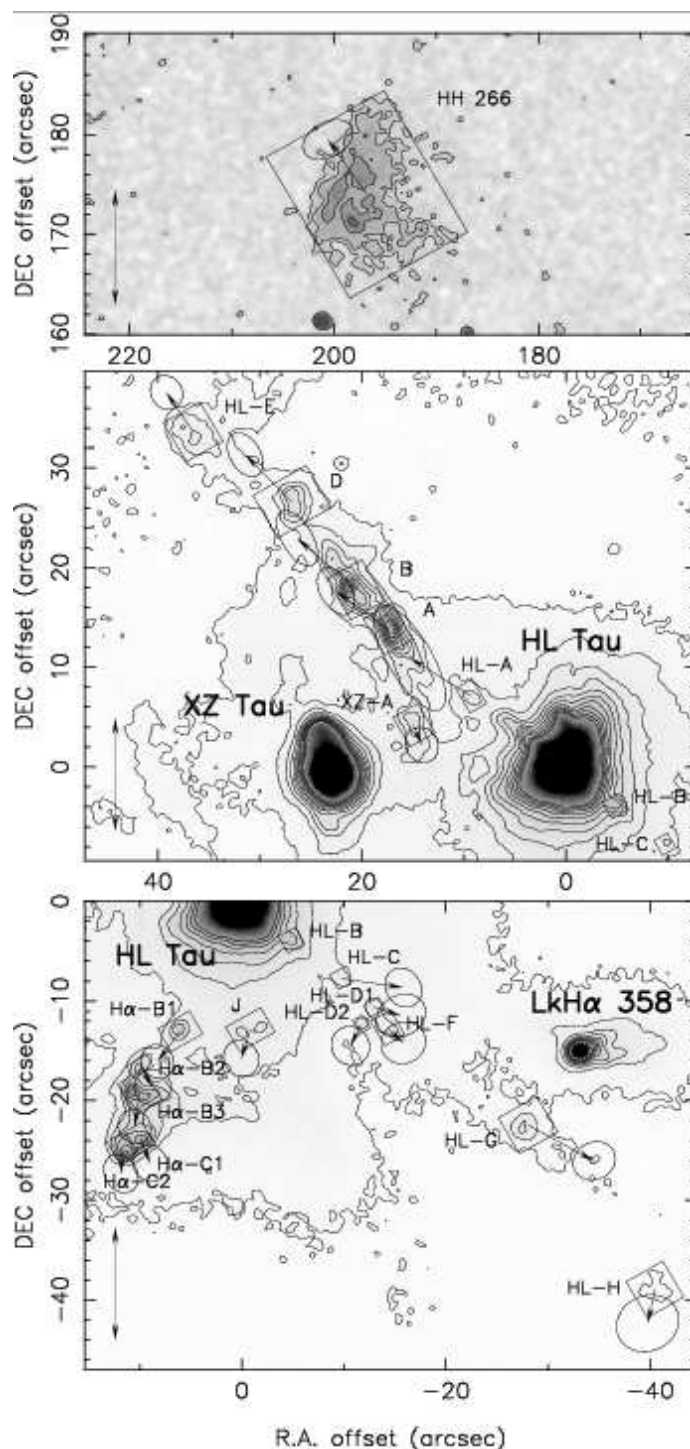


Fig. 6.— Proper motions of the HL/XZ Tau region and HH 266, shown on the NOT 1999 [SII] image. Lower panel shows the region south of HL Tau, central panel shows the HL Tau and XZ Tau jets, and upper panel shows HH 266. Axes are labeled in right ascension and declination offsets from the position of the HL Tau star. Arrows indicate the proper motion velocity of each knot. Ellipses at the end of each arrow indicate the uncertainty in the components of the velocity vector. The scale of the arrows is indicated by the double headed arrow shown in the bottom left corner of the map, corresponding to a velocity of 200 km s<sup>-1</sup>.

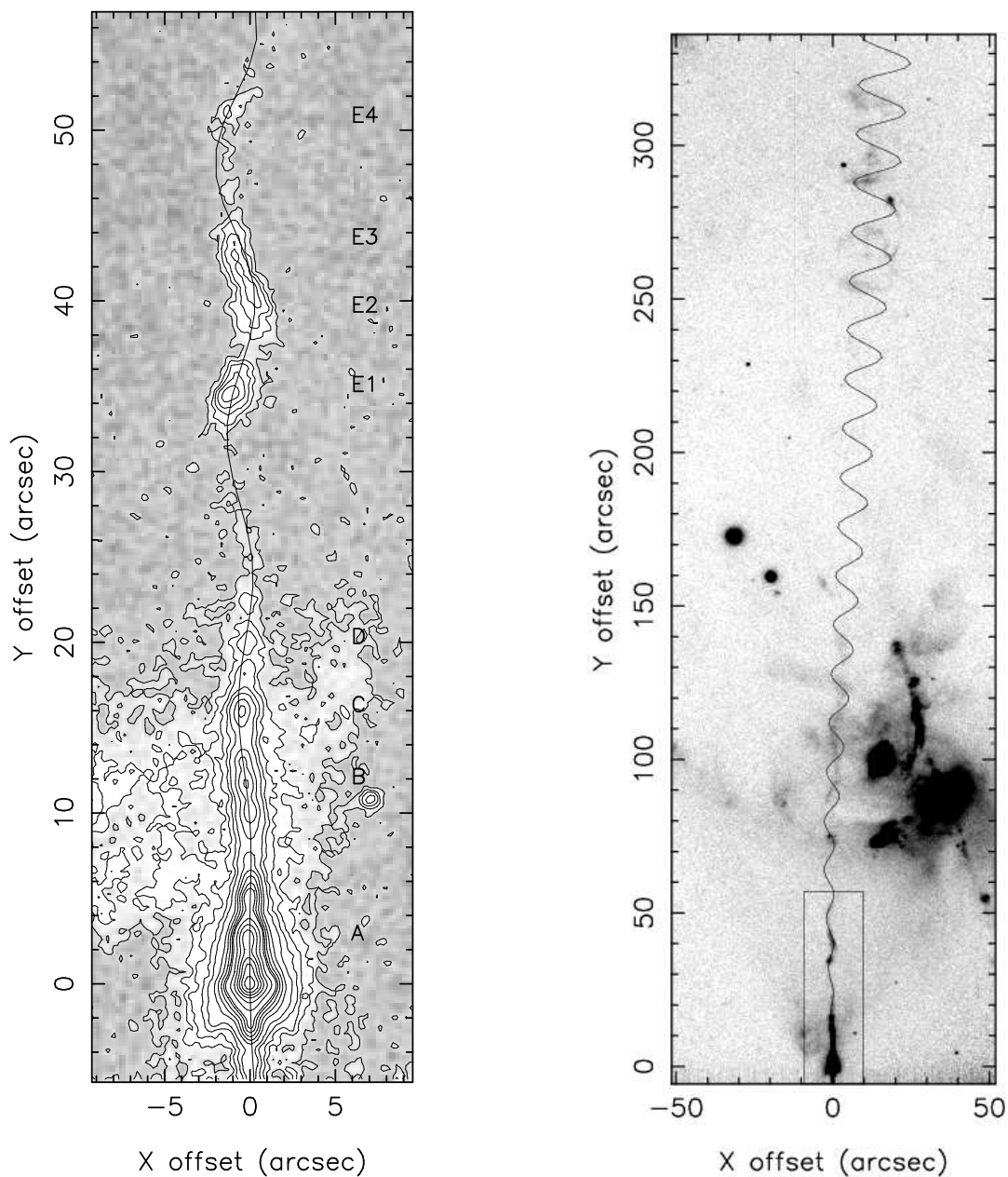


Fig. 7.— *(left)* NOT 1999 [SII] image of the A-E groups of knots of the HH 30 jet, with a fit of a ballistic jet shape overlaid. The parameters of the fit are P.A. =  $31^{\circ}6$ , half-opening angle  $\alpha = 1^{\circ}43$ , separation between maxima  $\lambda_y = 16''$ , and  $y_0 = 4''$ . *(right)* Same jet shape, but overlaid on the full image, extending up to HH 30-N. The P.A. changes in  $-5^{\circ}$  at a distance of  $72''$  from the source.

Table 1. Proper Motions of Knots in the HH 30 Jet

Knot	$y^a$ (arcsec)	$\mu_x$ (arcsec yr <sup>-1</sup> )	$\mu_y$ (arcsec yr <sup>-1</sup> )	$v_t^b$ (km s <sup>-1</sup> )	P.A. <sup>c</sup> (deg)
Z2	-4.5	-0.01 ± 0.06	-0.38 ± 0.06	255 ± 43	209 ± 8
Z1	-2.6	-0.02 ± 0.06	-0.10 ± 0.06	68 ± 43	196 ± 31
A0	0.0	-0.04 ± 0.06	0.01 ± 0.06	30 ± 38	101 ± 81
A1 <sup>d</sup>	1.0	...	...	...	...
A2	2.5	-0.01 ± 0.06	0.39 ± 0.06	260 ± 43	31 ± 8
A3	4.9	0.02 ± 0.06	0.32 ± 0.06	213 ± 43	26 ± 10
B1	10.0	0.02 ± 0.06	0.22 ± 0.06	145 ± 43	25 ± 15
B2	11.6	0.00 ± 0.06	0.42 ± 0.06	276 ± 43	29 ± 8
B3	13.0	0.01 ± 0.06	0.24 ± 0.06	160 ± 43	27 ± 13
C	15.8	0.02 ± 0.06	0.40 ± 0.06	268 ± 43	28 ± 8
D1	18.0	0.16 ± 0.06	0.49 ± 0.06	341 ± 43	12 ± 6
D2	19.7	0.15 ± 0.06	0.39 ± 0.06	275 ± 42	9 ± 8
E1	34.3	0.02 ± 0.04	0.29 ± 0.05	191 ± 33	26 ± 8
E2	38.9	0.08 ± 0.06	0.22 ± 0.05	158 ± 35	10 ± 15
E2+3	40.9	0.02 ± 0.04	0.21 ± 0.05	143 ± 33	24 ± 11
E3	42.9	-0.02 ± 0.05	0.22 ± 0.05	147 ± 36	35 ± 12
E4	49.9	0.13 ± 0.11	0.16 ± 0.14	136 ± 86	-8 ± 34
G1	72.2	0.17 ± 0.20	0.23 ± 0.05	190 ± 82	-7 ± 32
G1+2	73.3	-0.01 ± 0.05	0.15 ± 0.06	98 ± 38	35 ± 18
G2	74.1	-0.05 ± 0.06	0.12 ± 0.08	83 ± 50	53 ± 30
H1	89.0	0.01 ± 0.04	0.26 ± 0.05	172 ± 32	27 ± 10
H3	103.1	0.13 ± 0.08	0.16 ± 0.07	140 ± 46	-9 ± 19
H4	111.1	0.13 ± 0.10	0.22 ± 0.06	168 ± 49	-1 ± 21
I1	122.5	0.11 ± 0.12	0.20 ± 0.09	150 ± 64	2 ± 30
I2	133.6	-0.03 ± 0.06	0.28 ± 0.27	188 ± 180	36 ± 14
NA	251.4	0.02 ± 0.16	0.14 ± 0.10	92 ± 66	21 ± 64
NB	263.2	0.04 ± 0.05	-0.04 ± 0.06	34 ± 34	-105 ± 58
NC	268.7	-0.13 ± 0.15	0.42 ± 0.13	288 ± 88	47 ± 20
ND	278.9	-0.01 ± 0.04	0.07 ± 0.05	48 ± 30	37 ± 31
NE1 <sup>e</sup>	285.5	-0.02 ± 0.05	0.04 ± 0.05	34 ± 35	59 ± 59
NE2 <sup>e</sup>	285.5	-0.01 ± 0.05	0.09 ± 0.06	62 ± 38	36 ± 28
NF <sup>f</sup>	290.4	0.00 ± 0.04	-0.05 ± 0.05	34 ± 30	-147 ± 44

Table 1—Continued

Knot	$y^a$ (arcsec)	$\mu_x$ (arcsec yr <sup>-1</sup> )	$\mu_y$ (arcsec yr <sup>-1</sup> )	$v_t^b$ (km s <sup>-1</sup> )	P.A. <sup>c</sup> (deg)
NG1	293.3	0.06 ± 0.05	0.20 ± 0.06	139 ± 38	14 ± 13
NH	311.7	0.07 ± 0.04	0.11 ± 0.05	86 ± 32	-3 ± 20
NA-H <sup>g</sup>	282.4	-0.01 ± 0.04	0.18 ± 0.05	117 ± 35	33 ± 13

<sup>a</sup>Angular distance from the position of the brightest knot, A0, at  $\alpha(\text{J2000})=04^{\text{h}}31^{\text{m}}37^{\text{s}}.450$ ,  $\delta(\text{J2000})=+18^{\circ}12'25''.42$ , measured on the 1999 [SII] image along a direction with P.A. = 30°6, nearly coincident with the jet axis. The HH 30 star is estimated to be at  $y = -0''.51$  (Burrows et al. 1996; see text).

<sup>b</sup>Proper motion velocity, assuming a distance of 140 pc.

<sup>c</sup>Position angle with respect to the north direction.

<sup>d</sup>Knot A1 has only been identified in the 1999 image. No proper motion measurement is available.

<sup>e</sup>Knot NE has been split into two in order to minimize the effect of a clear morphology change between the two epochs in the proper motion measurement.

<sup>f</sup>The image of knot NF is very circular and compact, and its proper motion is compatible with zero. Most probably it is a field star.

<sup>g</sup>Box NA-H encompasses all the N knots, except the probable star NF.

Table 2. Spectroscopy of the HH 30 Jet<sup>a</sup>

Knot	$y^c$ (arcsec)	Size <sup>d</sup> (arcsec)	$v_{\text{hel}}^b$		$n_e$ ( $\text{cm}^{-3}$ )
			[SII] 6717 ( $\text{km s}^{-1}$ )	[SII] 6731 ( $\text{km s}^{-1}$ )	
F3	−8.5	4.4	14	16	630
A	0.0	11.2	16	16	3670
B	11.0	3.6	12	14	430
C	14.5	4.4	16	14	174
D	20.5	4.7	14	16	40
E1	34.5	3.3	14	20	< 10
E2+3	40.7	7.6	16	16	< 10
G	73.0	12.6	29	29	80
H1	87.4	2.9	29	25	...
H2	93.4	8.3	34	31	130
H3	105.0	6.8	36	38	< 10
H4	112.0	6.5	45	41	70
I1	119.0	3.2	47	...	...

<sup>a</sup>Line widths are smaller than the effective spectral resolution ( $\sim 32 \text{ km s}^{-1}$ ).

<sup>b</sup>Error is  $\sim 5 \text{ km s}^{-1}$ .

<sup>c</sup>Angular distance from knot A0 (see Table 1).

<sup>d</sup>Size of the region over which the spectra have been binned.

Table 3. Spectroscopy of HH 30-N<sup>a</sup>

Knot	$y^b$ (arcsec)	Size <sup>c</sup> (arcsec)	$v_{\text{hel}}^d$ (km s <sup>-1</sup> )	FWHM (km s <sup>-1</sup> )
NA	258	16.9	−96	103
NC <sup>e</sup>	274	5.4	−89	98
NE	286	7.5	−91	103
NG1	293	7.9	−73	112
NG2	303	5.4	−73	94
NH	312	7.2	−50	85

<sup>a</sup>Derived from the H $\alpha$  line.

<sup>b</sup>Angular distance from knot A0. H $\alpha$  spectroscopy data only provided position offsets between knots. The values of  $y$  have been estimated by assigning to knot NE the angular distance from knot A0 obtained from the 1999 [SII] image (Table 1).

<sup>c</sup>Size of the region over which the spectra have been binned.

<sup>d</sup>Error is smaller than  $\sim 10$  km s<sup>-1</sup>.

<sup>e</sup>The [SII] lines have been detected only for this knot, resulting in an electron density  $n_e = 380$  cm<sup>-3</sup>.

Table 4. Proper Motions of Knots in HL/XZ Tau and HH 266

Knot	$\Delta\alpha^a$ (arcsec)	$\Delta\delta^a$ (arcsec)	$v_t^b$ (km s <sup>-1</sup> )	P.A. <sup>c</sup> (deg)
HL-E	36.5	33.4	84 ± 31	34 ± 19
D	26.8	26.4	117 ± 42	44 ± 14
B	20.5	17.6	138 ± 52	48 ± 13
A	17.3	13.7	114 ± 43	53 ± 15
HL-A	9.2	6.9	126 ± 95	58 ± 27
HL-B <sup>d</sup>	-4.9	-3.9	...	...
HL-C	-9.7	-7.8	110 ± 33	-98 ± 18
HL-D1	-13.0	-10.6	49 ± 40	-108 ± 48
HL-D2	-11.7	-12.4	42 ± 33	154 ± 46
HL-F	-14.3	-12.7	38 ± 37	-134 ± 59
HL-G	-27.9	-22.5	132 ± 34	-119 ± 16
HL-H	-40.5	-38.9	62 ± 52	168 ± 49
J	-0.8	-12.9	54 ± 32	163 ± 34
H $\alpha$ -B1	6.0	-13.0	67 ± 28	144 ± 26
H $\alpha$ -B2	10.0	-16.5	44 ± 31	-150 ± 42
H $\alpha$ -B3	10.0	-19.1	62 ± 30	172 ± 27
H $\alpha$ -C1	9.9	-23.8	48 ± 33	201 ± 35
H $\alpha$ -C2	11.7	-24.8	45 ± 34	178 ± 39
XZ-A	14.9	4.2	38 ± 32	201 ± 42
HH 266	194.7	172.2	99 ± 36	43 ± 21

<sup>a</sup>Right ascension and declination offsets from the position of HL Tau, at  $\alpha(\text{J2000})=04^{\text{h}}31^{\text{m}}38^{\text{s}}.477$ ,  $\delta(\text{J2000})=+18^{\circ}13'58''.86$ , for the 1999 [SII] image.

<sup>b</sup>Proper motion velocity, assuming a distance of 140 pc.

<sup>c</sup>Position angle with respect to the north direction.

<sup>d</sup>Knot HL-B has only been identified in the 1999 image. No proper motion measurement is available.

Table 5. Comparison of Proper Motion Measurements in HL/XZ Tau

Knot	1987 <sup>a</sup>		1987–1999 <sup>b</sup>		1999 <sup>c</sup>	
	$v_t$ (km s <sup>-1</sup> )	P.A. (deg)	$v_t$ (km s <sup>-1</sup> )	P.A. (deg)	$v_t$ (km s <sup>-1</sup> )	P.A. (deg)
HL-E	319 ± 53	45 ± 4	204 ± 52	49 ± 15	84 ± 31	34 ± 19
D	299 ± 33	38 ± 3	178 ± 52	50 ± 17	117 ± 42	44 ± 14
B	226 ± 27	45 ± 3	162 ± 52	52 ± 18	138 ± 52	48 ± 13
A	146 ± 27	47 ± 3	180 ± 52	46 ± 16	114 ± 43	53 ± 15
HL-A	...	...	225 ± 52	34 ± 13	126 ± 95	58 ± 27
HL-B	...	...	24 ± 52	-134 ± 124	...	...
HL-C	...	...	196 ± 52	-137 ± 15	110 ± 33	-98 ± 18
HL-D1	...	...	121 ± 52	-139 ± 24	49 ± 40	-108 ± 48
HL-F	...	...	82 ± 52	19 ± 36	38 ± 37	-134 ± 59
HL-G	...	...	133 ± 52	-143 ± 22	132 ± 34	-119 ± 16
J	...	...	105 ± 52	-13 ± 28	54 ± 32	163 ± 34
H $\alpha$ -B1	...	...	128 ± 52	144 ± 23	67 ± 28	144 ± 26
H $\alpha$ -B2	...	...	25 ± 52	-24 ± 120	44 ± 31	-150 ± 42
H $\alpha$ -B3	126 ± 20	160 ± 7	49 ± 52	-93 ± 60	62 ± 30	172 ± 27
H $\alpha$ -C1	80 ± 20	97 ± 25	44 ± 52	-44 ± 67	48 ± 33	201 ± 35
H $\alpha$ -C2	80 ± 20	97 ± 25	62 ± 52	-37 ± 48	45 ± 34	178 ± 39
XZ-A	80 ± 33	76 ± 20	42 ± 52	52 ± 71	38 ± 32	201 ± 42

<sup>a</sup>From Table 4 of Mundt et al. 1990, scaled to a distance of 140 pc.

<sup>b</sup>From positions in Mundt et al. 1990 and in this paper. An error in position of 1'' is assumed for all knots.

<sup>c</sup>This paper.